

**Electroproduction of muon pairs with CLAS12: Double DVCS and J/ψ
electroproduction**

M. Guidal, E. Voutier, S. Niccolai, R. Dupre, C. Munoz, and D. Marchand

Institut de Physique Nucléaire d'Orsay, IN2P3, BP 1, 91406 Orsay, France

M. Battaglieri, A. Celentano, R. De Vita, E. Fanchini, M. Osipenko, M. Ripani, and M. Taiuti

Istituto Nazionale di Fisica Nucleare, Sezione di Genova e

Dipartimento di Fisica dell'Università, 16146 Genova, Italy

N. Liyanage, K. Gnanvo

University of Virginia, Charlottesville, VA 22904

M. Boer

P-25, Los Alamos National Laboratory, Los Alamos, NM 87545, USA

N. Baltzell, V. Burkert, L. Elouadrhiri, V. Kubarovský,

P. Nadel-Turonski, S. Stepanyan*, and M. Ungaro

Thomas Jefferson National Accelerator Facility, Newport News, Virginia 23606

R. Paremuzyan

University of New Hampshire

D. Sokhan

Glasgow University, Glasgow, Scotland

K. Joo, A. Kim, N. Markov, and D. Riser

University of Connecticut, Storrs, Connecticut 06269

M. Defurne, M. Garçon, H. Moutarde, S. Procureur, F. Sabatié

Irfu/SPhN, CEA, Centre de Saclay, F91191 Gif-sur-Yvette, France.

J.-A. Tan

Kyungpook National University, Daegu 41566, Korea

* Contact person

(Dated: June 4, 2016)

Abstract

In this letter we propose to study Generalized Parton Distributions of the proton using the Double Deeply Virtual Compton Scattering (DDVCS) process and nucleon gluonic structure using the electroproduction of J/ψ mesons in the threshold region. In order to avoid ambiguities and anti-symmetrization issues, we will study the DDVCS and the J/ψ production in the muon channel, $ep \rightarrow e'p'\gamma^*(J/\psi) \rightarrow e'p'\mu^-\mu^+$. The same final state is produced by a competing process, the Bethe-Heitler (BH), where the $\mu^-\mu^+$ pair is radiated by the incoming or scattered electron and not by the nucleon nor from the decay of a vector meson.

For DDVCS studies, as the BH cross section is in general largely dominating the DDVCS cross section at JLab kinematics, we will measure the Beam Spin Asymmetry (BSA) of the reaction resulting from the interference of the two processes. The amplitude of the BSA is proportional in a linear way to the proton GPDs. DDVCS provides an extra handle for the exploration of GPDs in the (x, ξ) plane thanks to the possibility to vary the invariant mass of the final muon pair. Furthermore, a change of sign of the BSA when the virtuality of the final timelike photon becomes larger than the virtuality of the initial spacelike photon is predicted. This should be a strong signature that the handbag mechanism and the basis of the GPD formalism is at play.

The J/ψ -electroproduction is a continuation of studies proposed in the experiment E12-12-001 but for incoming photon virtualities of $Q^2 > 0.1$ GeV 2 . The proposed measurements aim to study the center-of-mass energy (W), the squared-transferred-momentum (t) and the decay angular distributions of the J/ψ cross section for incoming photon virtualities up to $Q^2 \simeq 2.5$ GeV 2 in an uncharted region, close to the J/ψ production threshold.

For these studies a modified CLAS12 detector in Hall-B will be used with liquid hydrogen target and an 11 GeV longitudinally polarized electron beam. The muon pairs from time-like photon or J/ψ decay will be detected in the CLAS12 forward detector (FD). Scattered electrons will be measured in a new PbWO₄ calorimeter mounted in place of the CLAS12 high threshold Cherenkov counter. The kinematics of the recoil proton will be deduced from the missing momentum analysis of the $e'\mu^+\mu^-$ system. In addition to the PbWO₄ calorimeter, modifications to the CLAS12 will include GEM tracker in front of the calorimeter and a tungsten shielding installed behind the calorimeter. This arrangement will block CLAS12 FD from large flux of electromagnetic and hadronic backgrounds, and allows to run the detector at luminosities $\approx 10^{37}$ cm $^{-2}$ sec $^{-1}$. This setup essentially converts the CLAS12 forward detector into a muon detector. Besides the solenoid that provides a field to shield from Møller electrons, the CLAS12 central detector will not be used in this measurement. Total of 100 days is requested for the proposed studies as part of a new run group.

Contents

I. Introduction	4
II. Physics Motivation	6
A. Double Deep Virtual Compton Scattering	6
B. J/ψ Electroproduciton	16
III. Proposed Measurements	18
A. DDVCS	19
B. J/ψ production	20
C. Search for LHCb pentaquarks	22
D. Importance of the J/ψ measurements for the DDVCS studies	22
IV. Detector Configuration	23
A. PbWO_4 calorimeter	24
B. GEM tracker	29
C. Background studies and luminosity limits	31
1. Occupances in Forward DCs	31
2. Rates in GEM tracker	32
3. Rates in PbWO_4 calorimeter	33
D. Muon identification and trigger rates	33
1. Trigger rates	34
2. Identification of $e^-\mu^+\mu^-$ and accidental background	35
3. Muon energy loss and momentum resolution	38
E. Beam and Target	39
V. Cross Sections, Production Rates, and Expected Physics Results	40
A. DDVCS Cross Section and Expected Rates	40
B. J/ψ Electroproduction	47
C. Rates for pentaquarks	55
VI. Summary and Beam Time Request	62
References	63

I. INTRODUCTION

The program for studying Generalized Parton Distributions (GPDs) using the JLAB 12 GeV facilities consists of measuring spin (beam/target) observables and cross sections in Deeply Virtual Compton Scattering (DVCS) [1] and Deeply Virtual Meson Production (DVMP) [2], and the angular asymmetries in Timelike Compton Scattering (TCS) [3]. In these reactions, observables contain integrals of GPDs over the quark momentum fraction x (the real part of Compton amplitude) or GPDs at specific kinematical point, $x = \pm\xi$, (the imaginary part of Compton amplitude). In contrast, the Double Deeply Virtual Compton Scattering (DDVCS), where either the incoming and outgoing photon have large virtuality, allows to decorrelate the two variables and map out GPDs in a wide range of $x \neq \xi$, clearly yielding precious new information on GPDs, unaccessible otherwise. We propose to study beam-spin asymmetries in DDVCS using di-muon electroproduction, $ep \rightarrow e'\mu^+\mu^-p'$, in a wide range of space-like and time-like virtualities of incoming and outgoing virtual photons, respectively.

The same final state will allow to study J/ψ electroproduction. This process has been studied at high energies at HERA [4, 5] and FNAL [6]. Studies at large W showed some differences in behavior of J/ψ cross section in Q^2 compared to those for lighter vector mesons (e.g. cross section of the ρ production rises with W as W^δ , with $\delta \approx 0.2$ at $Q^2 = 0$ to $\delta \approx 0.8$ at $Q^2 = 30$ [7–9] while for J/ψ this parameter is ≈ 0.8 and almost independent of Q^2). There are no J/ψ electroproduction measurements at lower energies. The production mechanism close to threshold, $W < 4.5$ GeV, is poorly understood. Old photoproduction measurements indicate a cross section enhancement below 11 GeV photon energies with a behavior deviating from predictions of the 2-gluon exchange mechanism, which describes high energy data reasonably well. This observed deviation of the J/ψ production cross section from expectations necessitates studies with different probes and at different kinematics. We propose to measure W - and t -dependences of the cross section for incoming photon virtualities up to $Q^2 \simeq 2.5$ GeV 2 , as well as study decay angular distributions of muons in order to extract the ratio of longitudinal and transverse cross sections, $R = \sigma_L/\sigma_T$.

The J/ψ production reaction can also be used to search and study LHCb hidden charm pentaquarks in the electroproduction. The pentaquarks will be identified in the W distribution of events tagged with J/ψ . Expected W resolution will be sufficient for pentaquark searches.

The proposed experiment will study electroproduction of muon pairs in the reaction $ep \rightarrow e'\mu^+\mu^-p'$ using an 11 GeV longitudinally polarized electron beam, a liquid hydrogen target, and the modified CLAS12 detector in Hall-B. Measuring outgoing time-like photons and J/ψ -mesons

through their di-muon decays is chosen to addresses two important challenges of the measurements. First, contrary to the $\gamma^*(J/\psi) \rightarrow e^+e^-$ mode, the incoming/scattered and decay leptons are distinguishable. This eliminates ambiguity and anti-symmetrization issues for DDVCS, and reduces combinatorial background under the J/ψ peak in the lepton pair invariant mass distribution. Second, in order to accommodate the very small cross sections of both processes, the experiment has to run at much higher luminosity than the design luminosity, $\sim 10^{35} \text{ cm}^2 \text{ sec}^{-1}$, of the CLAS12 detector [10]. In order to run with orders of magnitude higher luminosities, the CLAS12 Forward Detector (FD) must be completely shielded from the electromagnetic and hadronic backgrounds. This shield in turn will work as an absorber/filter for the muon detector, i.e. CLAS12 FD. As will be shown below, in such configuration CLAS12 FD can run at luminosities of $\sim 10^{37} \text{ cm}^2 \text{ sec}^{-1}$. In the proposed setup scattered electrons will be detected in a compact, high resolution calorimeter ($PbWO_4$ crystal calorimeter), which will be part of the shield. There will be a tracking detector before the calorimeter/shield, capable of running in high rate, high occupancy environment, in order to help electron identification in the calorimeter and aid CLAS12 FD tracking system in reconstruction of the decay muons production vertex parameters. The estimated cost of the proposed modifications is $\sim \$4 \text{ M}$.

As will be shown below, the proposed setup will allow to collect data by triggering only on two minimum ionizing particles in CLAS12 Forward Detector in high luminosity running. This effectively converts it into a high rate $\mu\mu$ production factory. Clearly such setup opens up new opportunities for experiments such as vector meson production on nuclear targets, in particular J/ψ -meson production, in order to study $J/\psi N$ interaction, as an example.

II. PHYSICS MOTIVATION

A. Double Deep Virtual Compton Scattering

Double Deep Virtual Compton Scattering (DDVCS), stands for the reaction: $ep \rightarrow ep\gamma^* \hookrightarrow \ell^+\ell^-$, i.e. the exclusive electroproduction on the proton of a timelike photon which decays into a pair of leptons ℓ (muons in the present case).

It is a generalization of Deep Virtual Compton Scattering (DVCS): $ep \rightarrow ep\gamma$ (i.e. with a real photon in the final state) and Timelike Compton Scattering (TCS): $\gamma p \rightarrow p\gamma^* \hookrightarrow \ell^+\ell^-$ (i.e. with a real photon in the initial state). For virtualities of the virtual photons large enough ($Q^2 = (e - e')^2$ for DVCS or $Q'^2 = (\ell^+ + \ell^-)^2$ for TCS) and small nucleon momentum transfer $t = (p - p')^2$, it has been shown that these reactions are probing the internal quark and gluon structure of the nucleon via the formalism of the Generalized Parton Distributions (GPDs). See Refs. [11–14] for reviews on the subject of GPDs and DVCS and Refs. [15–17] for studies of TCS. In Fig.1 diagrams of the DVCS, TCS and DDVCS processes are presented. These so-called “handbag” diagrams illustrate the QCD factorization theorem behind the formalism of GPDs: in the Bjorken regime, the processes are the (convolution) product of a hard scattering part exactly calculable in QED, i.e. the elementary photon-quark scattering $\gamma q \rightarrow \gamma q$, and soft non-perturbative QCD matrix elements, called the GPDs for their momentum space representation.

There are four GPDs, called $H, \tilde{H}, E, \tilde{E}$, which enter the DVCS amplitude at leading twist QCD and reflect the four independent quark-nucleon helicity-spin transitions between the initial and final states. They depend upon three variables : x , ξ and t . As illustrated in Fig. 1, $x + \xi$ is the *longitudinal* momentum fraction carried by the initial quark struck by the spacelike virtual photon, and $x - \xi$ is *longitudinal* momentum fraction carried by the final quark going back in the nucleon after radiating a photon. In Ji’s notation [18], the variable x varies between -1 and 1 while ξ varies between 0 and 1 (due to time reversal invariance, the range of ξ can be reduced to this range). One way to interpret the GPDs is therefore as the probability amplitude of finding a quark (if $x > \xi$, or an antiquark if $x < -\xi$) in the nucleon with a longitudinal momentum fraction $x + \xi$ and of putting it back into the nucleon with a longitudinal momentum fraction $x - \xi$ plus some transverse momentum “kick” to the target, which is represented by t . One can note the interesting region $-\xi < x < \xi$ where one “leg” in Fig. 1 has a positive momentum fraction (a quark) while the other one has a negative one (an antiquark). In this region, GPDs behave like a meson distribution amplitude and can be interpreted as the probability amplitude of finding a quark-antiquark pair in the nucleon. At $\xi = 0$, t can be interpreted as the conjugate variable of the *transverse* impact

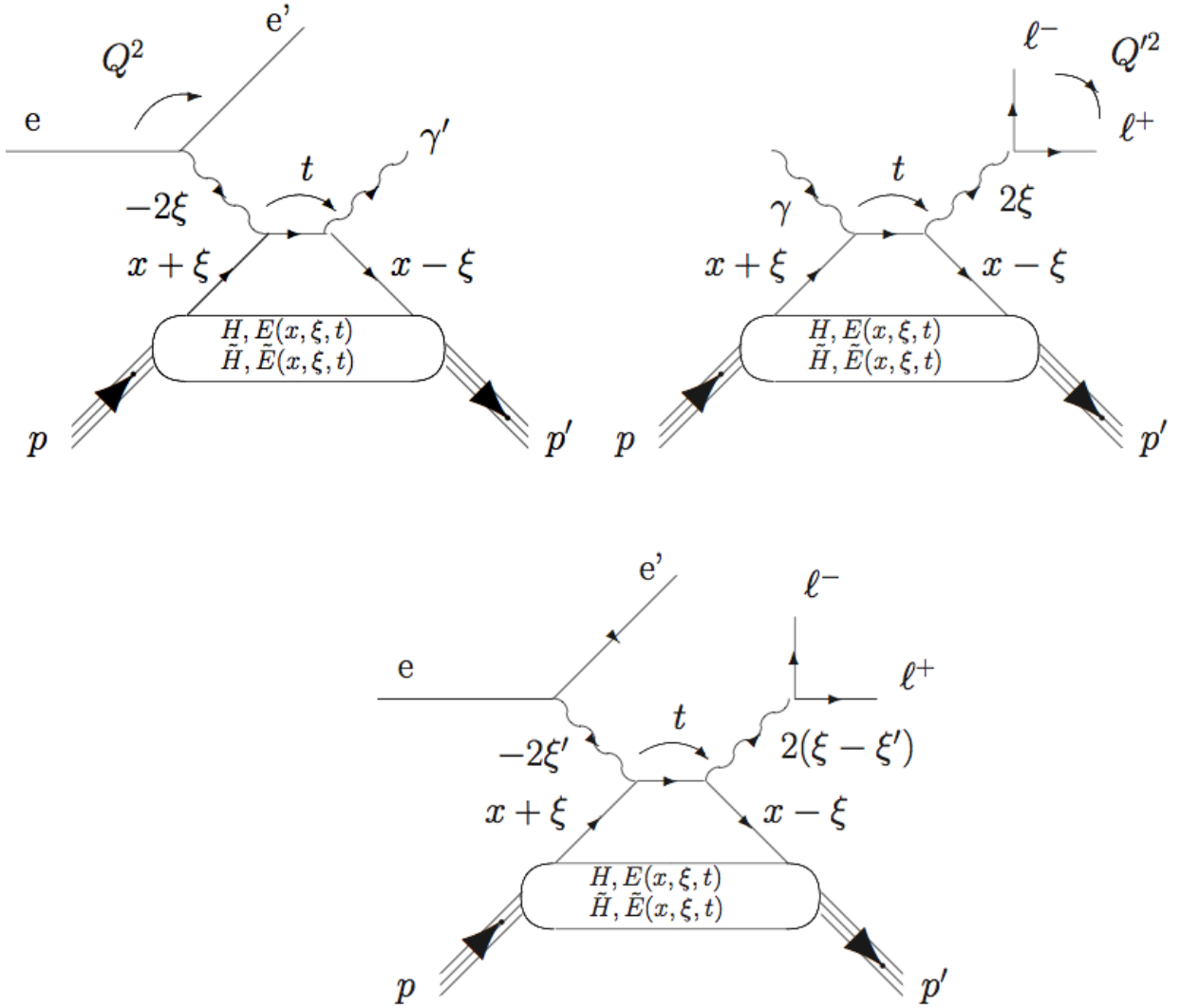


FIG. 1: Top left: DVCS handbag diagram. Top right: TCS handbag diagram. Bottom: DDVCS handbag diagram. Only “direct” diagrams are shown. There are also “crossed” diagrams, where the initial photon hits the final quark and vice-versa. In a frame where the nucleon moves at the speed of light along a certain direction, the longitudinal momentum fractions of the particles are also indicated.

parameter b_\perp and GPDs describe then the probability amplitude of finding in a nucleon a parton with a *longitudinal* momentum fraction x at a given *transverse* distance b_\perp from the center of the nucleon.

Fig. 2 shows, according to one particular GPD model (VGG [11, 19]), how the (x, ξ) and the

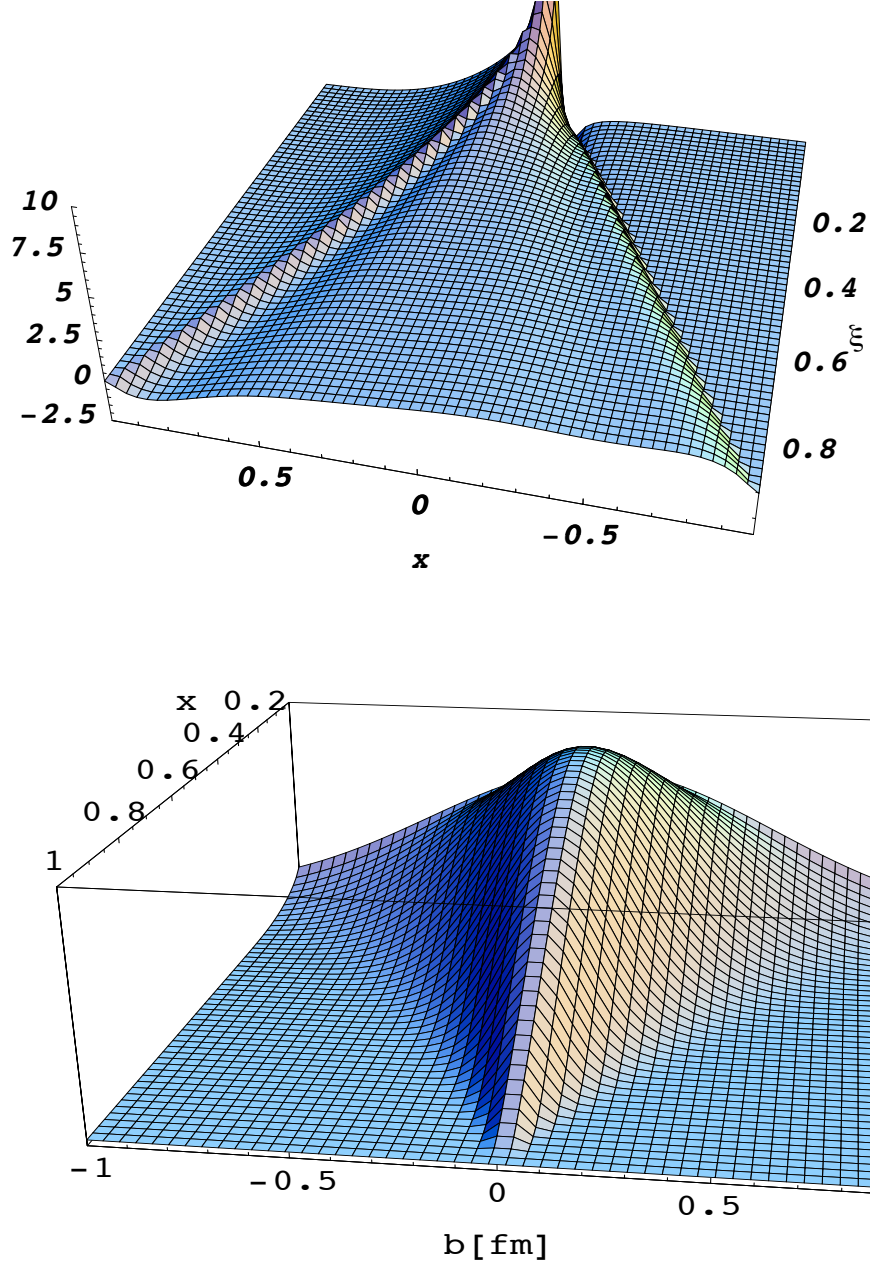


FIG. 2: Top: the GPD $H^u(x, \xi, t)$ as a function of the *longitudinal* momentum fraction x and the *longitudinal* momentum transfer ξ at $t = 0$ according to the VGG model. One recognizes for $\xi=0$ the typical shape of a parton distribution (with the sea quarks rising as x goes to 0, the negative x part being interpreted as the antiquark contribution) and as ξ increases the (asymptotic) shape of a distribution amplitude. Bottom: the GPD $H^u(x, \xi, t)$ as a function of the *longitudinal* momentum fraction x and the *transverse* impact parameter b_\perp (the conjugate variable of t) at $\xi = 0$ according to the VGG model

(x, b_\perp) correlations could appear. It shows the richness and novelty of the GPDs: information on $q\bar{q}$ configurations in the nucleon, correlations between quarks (or antiquarks) of different momenta, correlations between longitudinal momentum and transverse position of partons (nucleon “tomography”).

A crucial issue in the GPD formalism is the dependence on three variables, x , ξ and t , while only two of these three variables are accessible experimentally, ξ and t . In DVCS, ξ is approximated as $\xi = \frac{x_B}{2-x_B}$, fully defined by detecting the scattered lepton, and in TCS, ξ is approximated as $\xi = \frac{Q'^2}{2s-Q'^2}$, fully defined by detecting the final leptons.

The squared momentum transfer t is defined both in DVCS and in TCS by detecting either the recoil proton or the outgoing photon. The variable x is however integrated over in both the DVCS and TCS amplitudes, due to the loop in the “handbag” diagrams (see Fig. 1). Precisely, the DVCS amplitude is proportional to:

$$\int_{-1}^{+1} dx \frac{H(x, \xi, t)}{x - \xi + i\epsilon} + \dots \quad (1)$$

(where the ellipsis stand for similar terms in E , \tilde{H} and \tilde{E}). The $\frac{1}{x - \xi + i\epsilon}$ term is the propagator of the quark between the incoming virtual photon and the outgoing photon. The previous expression can be decomposed into real and imaginary parts:

$$PV\left(\int_{-1}^{+1} dx \frac{H(x, \xi, t)}{x - \xi}\right) - i\pi H(\xi, \xi, t) \quad (2)$$

This means that the maximum information that can be extracted from the experimental data at a given (ξ, t) point is $H(\pm\xi, \xi, t)$, when measuring an observable particularly sensitive to the imaginary part of the DVCS amplitude (such as single beam or target spin asymmetries), and $\int_{-1}^{+1} dx \frac{H(\mp x, \xi, t)}{x \mp \xi}$, when measuring an observable particularly sensitive to the real part of the DVCS amplitude (such as unpolarized cross sections or double-spin beam/target spin asymmetries).

Experimentally, DVCS is accessed by measuring the reaction $ep \rightarrow e p \gamma$ and TCS by measuring the reaction $\gamma p \rightarrow p \ell^+ \ell^-$. However, DVCS and TCS are not the only processes leading to these final states. There are also the so-called Bethe-Heitler (BH) processes. In $ep \rightarrow e p \gamma$, BH produces a final state photon radiated either from the incoming or the scattered electron, while in $\gamma p \rightarrow p \ell^+ \ell^-$ the final lepton pair originates from the photon beam (see Fig. 3). In both cases, the final state photon (be it real or virtual) doesn’t originate from the nucleon and therefore does not carry any partonic or GPD information. The BH interferes with DVCS (and TCS) at the amplitude level and therefore complicates the extraction of the DVCS and TCS (i.e. GPDs) information. However, it is rather precisely calculable theoretically and can be put under control.

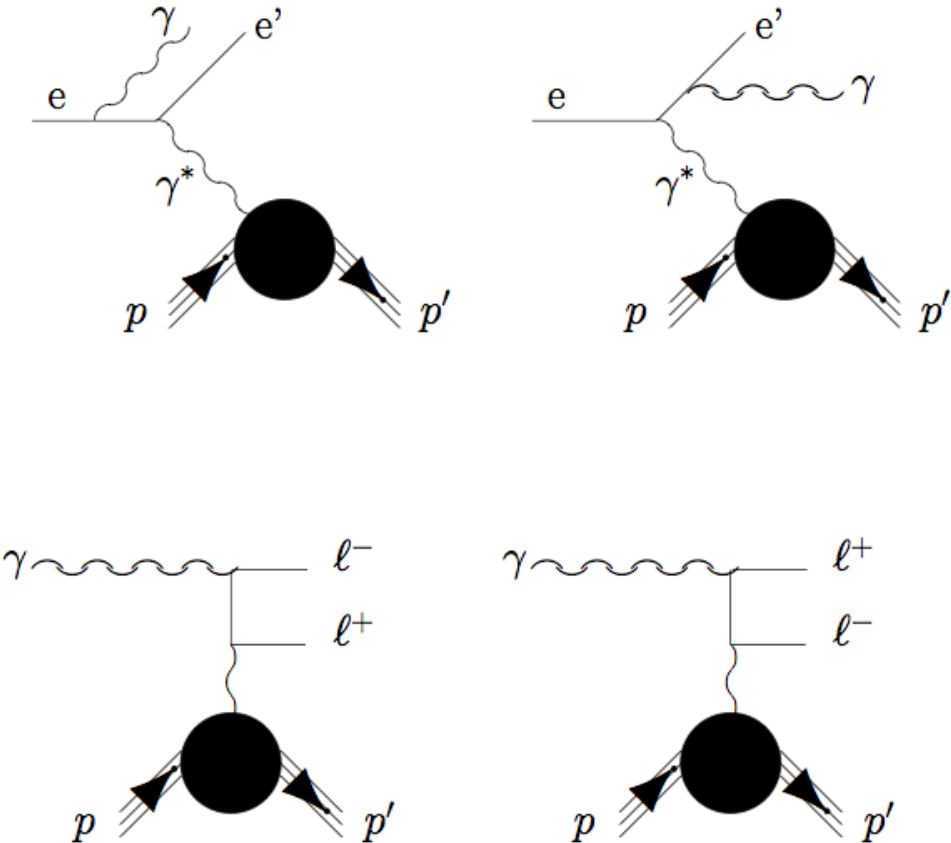


FIG. 3: Top: the BH diagrams for DVCS. Bottom: the BH diagrams for TCS. In DDVCS, all four contributions are present (the DVCS-BH diagrams have to be “completed” by the decay into a lepton pair of the final state photon and in the TCS-BH diagrams, the initial state real photon must emerge from an electron beam).

While no experimental data have been published related to TCS (and DDVCS), quite some data has already been released related to DVCS (on the proton). Limiting oneself to the valence (JLab) region, unpolarized cross sections [20–22], beam spin asymmetries [23] and longitudinally polarized target spin asymmetries as well as double spin beam-target asymmetries [24–26] have been measured.

These past few years, several groups [27–32] have developed fitting codes and algorithms aimed at extracting the GPD information from these DVCS data. The complexity of the task is due to, in particular, the BH contribution in addition to DVCS. These fitting algorithms have nevertheless succeeded in extracting the quantities $H(\pm\xi, \xi, t)$ and $\tilde{H}(\pm\xi, \xi, t)$ at the $\approx 30\%$ level for different

values of ξ and t (see Ref. [14] for a compilation of the fit results). Although the information thus obtained is already very valuable and provides first constraints on GPD models, it is very desirable to extract the quantities where the first two arguments of the GPDs, x and ξ , are decoupled (i.e. $x \neq \xi$). For instance, “nucleon imaging” requires the knowledge of $H(\xi, 0, t)$, and similarly for the other GPDs (only for $\xi = 0$, the GPDs have a probabilistic interpretation [33]). With results from DVCS (and TCS) alone, a model-dependent correction procedure has to be applied to extrapolate from $H(\xi, \xi, t)$ to $H(\xi, 0, t)$.

The way to avoid the x -integration issue is DDVCS. Compared to DVCS, DDVCS contains an additional kinematic lever arm with the timelike virtuality of the final photon which can now be varied (by measuring the invariant mass of the decay leptons pair). Fig. 1 illustrates this where the *plus*-components (in light-cone kinematics) of the longitudinal momentum fraction of the quarks and photons are indicated. In the DDVCS case, the kinematics of the 2 photons (incoming and outgoing) are described by 2 variables, ξ and ξ' , which can be independently varied (whereas, in DVCS, only ξ can be varied). For DDVCS, there are two diagrams (only the “direct” one is shown in Fig. 1) and their propagators read:

$$\frac{1}{x - (2\xi' - \xi) + i\epsilon} + \frac{1}{x + (2\xi' - \xi) - i\epsilon} \quad (3)$$

Therefore, the DDVCS amplitude is proportional to:

$$\int_{-1}^{+1} dx \frac{H(x, \xi, t)}{x - (2\xi' - \xi) + i\epsilon} + \dots \quad (4)$$

By measuring an observable proportional to the imaginary part of the DDVCS amplitude (for instance, the beam spin asymmetry, like in the DVCS case), one has access, in a concise notation, to $H(2\xi' - \xi, \xi, t) + H(-(2\xi' - \xi), \xi, t)$ (keeping the contribution of the crossed term of Eq. 3. We refer the reader to Refs. [34–36] for the details of the formalism. This therefore allows for mapping the GPD’s along each of the three axis (x , ξ and t) as the three variables can now be varied independently. An important restriction is that, in DDVCS, only the region $0 < 2\xi' - \xi < \xi$ can be accessed. This is called the ERBL region which provides information about the mesonic components of the nucleon. One can be sensitive to the complementary region, the so-called DGLAP region, when two spacelike virtual photons are involved, i.e. $ep \rightarrow ep$ elastic scattering with 2-photon exchange.

Experimentally, $\xi' = \frac{x_B}{2-x_B}$, i.e. it is fully defined by the detection of the scattered electron, and $\xi = \xi' \frac{Q^2 + Q'^2}{Q^2}$, i.e. it requires in addition the determination of the (squared) invariant mass of the lepton pair Q'^2 . In other words, if one fixes x_B , one defines uniquely ξ' and if one fixes Q^2 and Q'^2

according to the combination in the previous sentence, one defines uniquely ξ . In order to access the combination $H(2\xi' - \xi, \xi, t) + H(-(2\xi' - \xi), \xi, t)$, one should thus aim at measuring the DDVCS beam asymmetry at fixed x_B , Q^2 and t for a series of Q'^2 values (one can actually also vary Q^2 , as long as the combination $\frac{Q^2+Q'^2}{Q^2}$ remains constant so as to keep $2\xi' - \xi$ fixed).

Fig. 4 shows for instance the predicted beam spin asymmetries for the DDVCS process at typical JLab beam energies for different Q'^2 values. This asymmetry arises from the interference between the DDVCS and associated Bethe-Heitler processes, which are a generalization of the four diagrams of Fig. 3 (the final state real photon of the “DVCS-BH” diagrams is to decay into a lepton pair and the initial state real photon of the “TCS-BH” diagrams is to be radiated from an electron beam). One recognizes the familiar sinusoidal-like shapes as a function of ϕ , the azimuthal angle between the leptonic and hadronic planes. We also recall that only $Q'^2 = 0$ can be accessed in DVCS. The dependence on Q'^2 reflects the variation of the first argument of the GPD ($x = 2\xi' - \xi$) for a given second argument ξ . Fig. 4 shows that there is a strong sensitivity which should ultimately allow the extraction of the GPDs in the (x, ξ) plane.

In Fig. 4, it is very interesting to note the change in sign of the beam spin asymmetry as one goes from the region $Q'^2 < Q^2$ to the region $Q'^2 > Q^2$. It can be said that one goes from the “spacelike-dominated” region to the “timelike-dominated” region, or from the “DVCS-dominated” region to the “TCS-dominated” region. It was shown in Ref. [37] that the TCS amplitude is the conjugate of the DVCS amplitude. One can therefore understand the change in sign of the beam spin asymmetry in Fig. 4 as one crosses the $Q^2 = Q'^2$ region as a change in sign of the imaginary part of the DDVCS amplitude. This is a prediction of the “handbag” formalism and a very strong test that one is in the right regime to access GPDs. One should note that the region around $Q'^2 = Q^2$ might not be directly applicable to the GPD formalism. Indeed, in this region, the quark in the propagator of the DDVCS diagram in Fig. 1 has a momentum close to 0 as $Q'^2 = Q^2$ is essentially equivalent to $2\xi' - \xi = 0$. Therefore, pQCD factorization will break down and soft scales mechanisms will enter into play. Even though this particular region $Q'^2 = Q^2$ might not be directly interpretable in terms of GPDs, it is extremely interesting to make measurements at those kinematics to understand the transition between soft and hard mechanisms.

Fig. 5 shows the range in $2\xi' - \xi$ that can be accessed at the particular kinematics: $E_e=11$ GeV, $x_B=0.15$ (i.e. $\xi \approx 0.8$), $Q^2=2.75$ GeV 2 and $-t=0.3$ GeV 2 , by varying Q^2 from 1 to 7 GeV 2 . In particular one can note the (anti-)symmetry (oddness) around $2\xi' - \xi$ which reflects the quasi (anti-)symmetric behavior of the beam spin asymmetry of Fig. 4 around $Q^2 = Q'^2$. One has therefore two relatively independent ways of measuring the same combination of GPDs $H(2\xi' -$

$\xi, \xi, t) + H(-(2\xi' - \xi), \xi, t)$: in the region $Q^2 < Q'^2$ and in the region $Q^2 > Q'^2$. Only the sign of the combination varies as one amplitude is the conjugate of the other.

The downside of the DDVCS process is however the very low cross section involved. Indeed, due mainly to the extra $\alpha_e \approx 1/137$ coupling introduced by the decay of the outgoing photon into the lepton pair, the cross section is about a factor 300 [34] less than the DVCS process, at $Q'^2 \approx .3$ GeV² for instance.

We recall that the beam spin asymmetry for DVCS has been measured [23] for ≈ 60 (x_B , Q^2 , t) bins with the JLab 6 GeV beam and the CLAS detector with a luminosity of $10^{34}\text{cm}^{-2}\text{s}^{-1}$. As we will be shown in the following of this document, it is anticipated to run with the JLab 12 GeV beam and the CLAS12 detector at a luminosity of $10^{37}\text{cm}^{-2}\text{s}^{-1}$. Intuitively, it can therefore be anticipated that the DDVCS beam spin asymmetry measurement will be feasible, taking also into account an extra factor for the final state lepton pair detection efficiency.

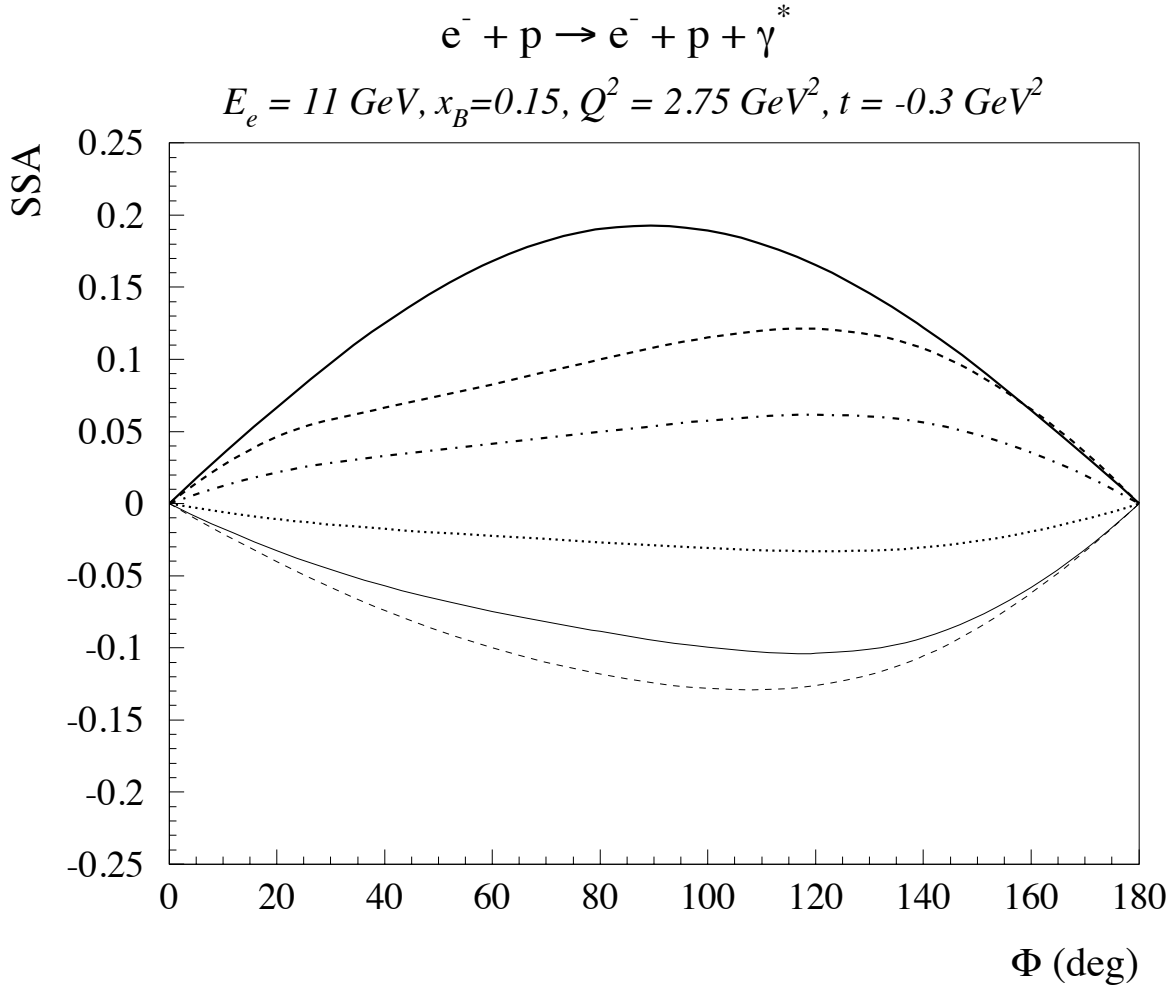


FIG. 4: Beam spin asymmetry for the reaction $ep \rightarrow e' p \mu^+ \mu^-$ (DDVCS+BH) for different virtualities of the lepton pair : $Q'^2 = 0.$ (thick solid line), which corresponds to a DVCS calculation, 1.5 (thick dashed line), 2. (thick dash-dotted line), 2.8 (dotted line) 3.6 (thin solid line) and 4.4 GeV^2 (thin dashed line). Calculations and predictions from [34]. The kinematics has been integrated over the 2 decay angles.

$$x_B = 0.15, Q^2 = 2.75 \text{ GeV}^2, t = -0.3 \text{ GeV}^2$$

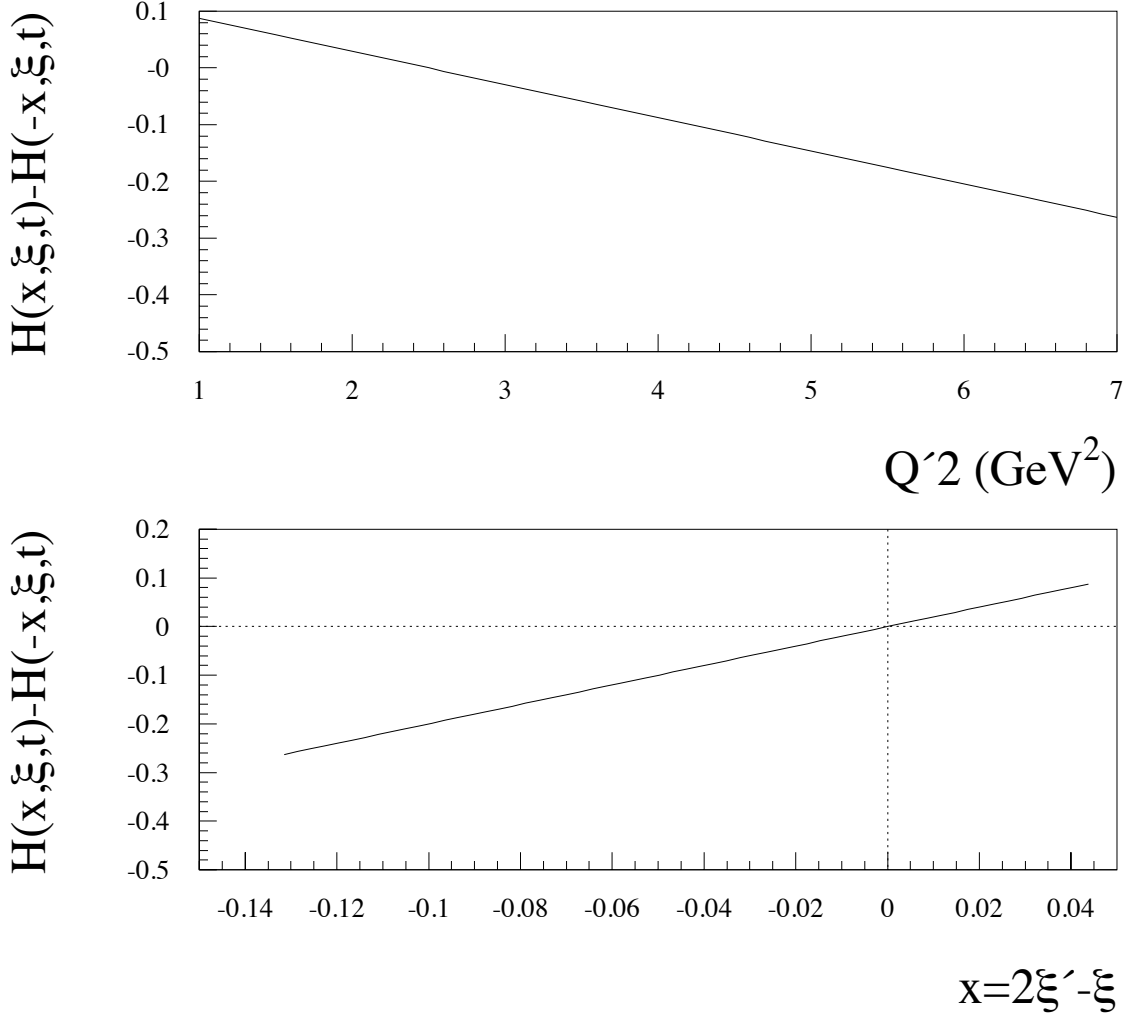


FIG. 5: Assuming the dominance of the H GPD in the DDVCS beam spin asymmetry, the GPD combination $H(2\xi' - \xi, \xi, t) + H(-(2\xi' - \xi), \xi, t)$ that can be accessed, as a function of Q'^2 (top panel) or equivalently $2\xi' - \xi$ (bottom panel), for fixed ξ' (i.e. x_B) and fixed t . In the bottom panel, the negative $2\xi' - \xi$ region allows to access the $-(H(2\xi' - \xi, \xi, t) + H(-(2\xi' - \xi), \xi, t))$ GPD combination for positive $2\xi' - \xi$, due to the symmetry of the problem.

B. J/ψ Electroproduciton

While J/ψ electroproduction at high energies has been studied well at HERA [4, 5] and FNAL [6], and a detailed program of “gluon imaging” along these lines is planned with a future Electron Ion Collider (EIC) [38], measurements of J/ψ electroproduction near threshold ($W = 4.04$ GeV) are lacking. The J/ψ production near threshold is a rich and complex physics topic in its own right and presently the subject of intense theoretical research. The measurement of the J/ψ electroproduction cross section is of great interest for the purpose of a precise yield extraction. Below is the current understanding of J/ψ production near threshold, and the role of the J/ψ measurement in the present experiment.

The production of heavy quarkonia and their interaction with hadronic matter are key questions of QCD, which are being studied through production experiments at different energies and various theoretical approaches; see Ref. [39] for a recent review. Because of the small spatial size of heavy quarkonia on the hadronic scale, $r_{Q\bar{Q}} \ll 1$ fm, one can use QCD operator methods to describe their interactions with hadrons and external probes in controlled approximation. Heavy quarkonium production probes the local color (gluon) fields in the nucleon, and can reveal properties such as their response to momentum transfer, their spatial distribution, and their correlation with valence quarks. The dynamics that produces the relevant gluon fields in the nucleon changes considerably between high energies and the near-threshold region, creating a fascinating landscape that calls for detailed experimental study. At high energies ($W > 10$ GeV) exclusive J/ψ photo- and electroproduction probes the nucleon’s gluon GPD at small momentum fractions $x \sim M_{J/\psi}^2/W^2 \ll 1$ and can be used to infer the transverse spatial distribution of small- x gluons in the nucleon, Fig.6.a; see Ref. [40] for a review. In exclusive J/ψ production near threshold, the minimum invariant momentum transfer to the nucleon becomes large: $|t_{\min}| = 2.23$ GeV² at threshold. The process is therefore analogous to elastic eN scattering at large $|t|$, except that the “probe” couples to the gluon field in the target, Fig.6.b. Exclusive J/ψ production near threshold thus measures the nucleon form factor of a gluonic operator and can provide unique information on the non-perturbative gluon fields in the nucleon.

The precise identification of the gluonic operators associated with J/ψ production near threshold and the modeling of their nucleon form factors are the subject of intense theoretical research, the status and perspectives of which were summarized at a recent topical workshop [41]. Several approaches are presently being discussed. One scenario assumes that even near threshold the J/ψ is produced through two-gluon exchange with a GPD-like coupling to the nucleon, but now in the

special kinematics of large $|t| \sim |t_{\min}|$ and large “skewness” $\xi \sim 0.5$ [42]. A more likely possibility is that the production process near threshold effectively reduces to a local gluonic operator, implying simple kinematic scaling relations [41]. Another scenario uses the hard scattering mechanism for high- t elastic form factors and assumes that the production process happens in the leading 3-quark Fock component of the nucleon, with rescattering through hard gluon exchange [43]. The J/ψ production near threshold is also being studied in the non-relativistic QCD (NRQCD) scheme, which attempts a systematic parametric expansion in the heavy quark velocity [44, 45]; first results for JLab 12 GeV kinematics were reported in Ref. [46].

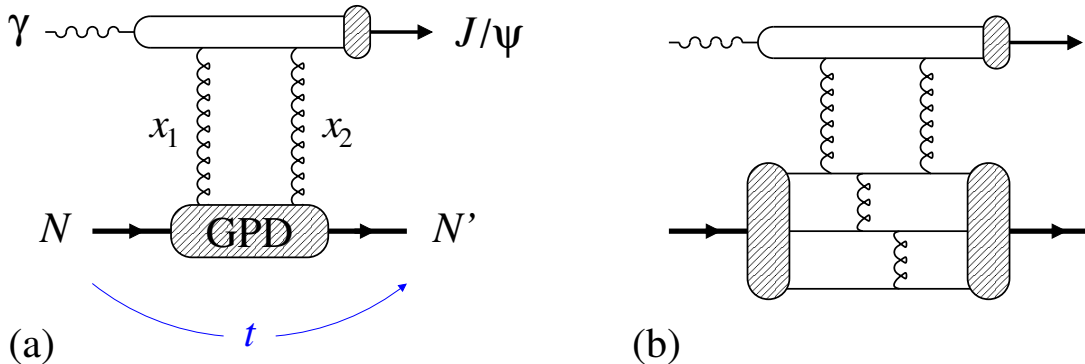


FIG. 6: .

It is clear that progress with unraveling the mechanism of J/ψ production near threshold depends crucially on experimental input. Because of the small cross sections exclusive J/ψ production near threshold has never been measured with the precision necessary to discriminate between the proposed dynamical scenarios, let alone to extract quantitative information on the relevant operators probing the color fields in the nucleon. There is already approved experiment with CLAS12 to explore J/ψ photoproduction in the unmeasured near-threshold region from $E_\gamma \approx 8.5$ GeV to 11 GeV. The projected data of [47] will dramatically extend and improve our knowledge of the J/ψ photoproduction cross section and t -dependence near threshold and directly impact on the on-going theoretical studies of the reaction mechanism. In this measurement, studies will focus on Q^2 dependence of the t -dependence of the differential cross section as well as the ratio $R = \sigma_L / \sigma_T$ via analysis of decay angular distributions of final state muons.

III. PROPOSED MEASUREMENTS

The experiment will measure production of muon pairs in (ep) scattering with 11 GeV electrons, see Figure 7. The reaction -

$$ep \rightarrow e' \mu^+ \mu^- p' \quad (5)$$

will be studied in wide range of W , Q^2 , t , and $M_{\mu\mu}$ (Q'^2). We intend to detect scattered electrons and the muon pairs, the recoil proton will be reconstructed in the missing momentum analysis. As was mentioned above and will be described below, a modified CLAS12 detector in Hall-B will be used for this measurement. Modifications include electromagnetic calorimeter installed in front of the CLAS12 Forward Detector for detection and identification of electrons in polar angular rage from 7° to 30° with momenta $p > 0.5$ GeV. A tungsten shield/absorber will follow the calorimeter and will play a dual role, as a shield for CLAS12 FD from large electromagnetic and hadronic backgrounds produced in the target, and as an absorber for charged hadrons (mostly pions) in front of the muon detector, i.e. the CLAS12 FD. There will be tracking detector before shield/calorimeter that will aid reconstruction of vertex parameters of e^- , μ^+ , and μ^- .

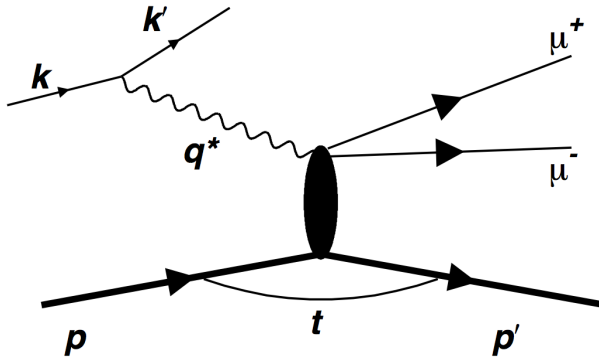


FIG. 7: Diagram of the muon pair electroproduction.

Kinematic coverage of the experiment when scattered electron kinematics is constrained within expected detection range of the calorimeter is shown in Figure 8. Events in these distributions are simulated according to $1/Q^4$ and e^{3t} dependancies, where $Q^2 = -q^2 = -(k - k')^2$ and $t = (p' - p)^2$. Here k (k') is the four vector of the incoming (scattered) electron and p (p') is the four vector of the target (recoil) proton. The invariant mass of muon pairs, $M_{\mu^+\mu^-} = (p_{\mu^+} + p_{\mu^-})^2$, was simulated according to the phase space (the p_μ is the four momentum of decay muons). The beam energy of 11 GeV sets the limit on $W^2 = (q + p)^2$ and $M_{\mu^+\mu^-}$. The reach in Q^2 and t is rate limited and will be discussed below.

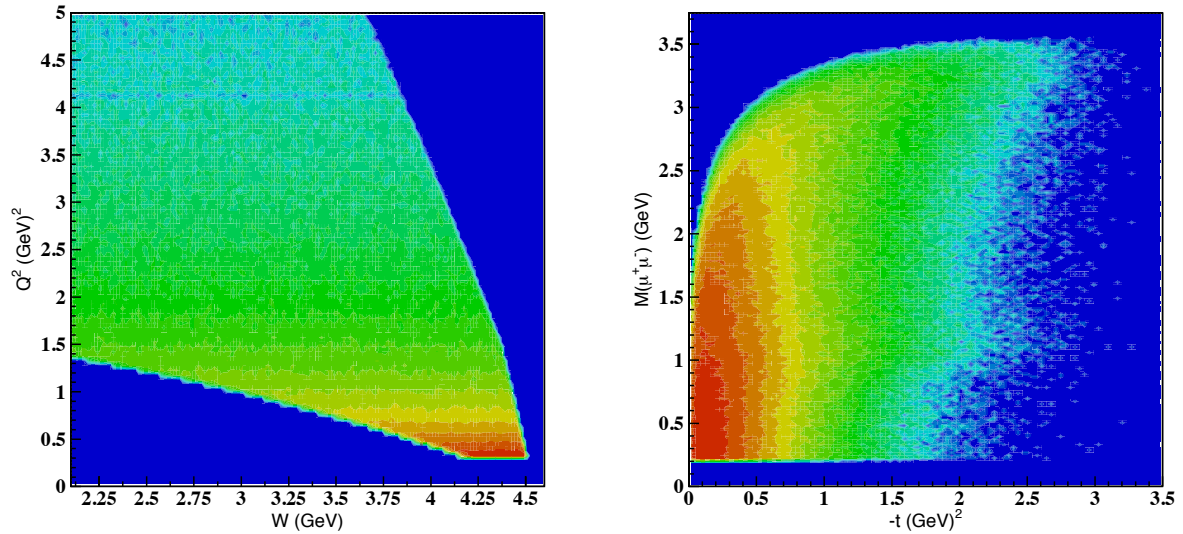


FIG. 8: Kinematical coverage of di-muon electroproduction experiment. Left, Q^2 vs. W distribution for (ep) scattering at 11 GeV when scattered electron is detected in the polar angular range from 7° to 30° with momenta $p > 0.5$ GeV. On the right, the invariant mass of lepton pair vs. squared transferred momentum for the same selection. Events were simulated with dependancies of $1/Q^4$ and e^{3t} , and the lepton pair mass distribution according to phase space.

A. DDVCS

In the DDVCS experiment, the main goal is to measure Beam Spin Asymmetries (BSA) as a function of lepton and hadron scattering planes, Φ_L , in a wide range of $Q'^2 \equiv M_{\mu\mu}^2$ and Q^2 , which will allow to “scan” over Q'^2 (keeping Q^2 fixed) and observe whether the asymmetry changes sign going from $Q'^2 < Q^2$ region to $Q'^2 > Q^2$. Here BSA asymmetry is defined as

$$Asym = \frac{1}{p_b} \frac{N^+ - N^-}{N^+ + N^-} \quad (6)$$

where N^- and N^+ are number of events with negative and positive beam helicities, respectively, and p_b is the beam polarization. In particular in Fig.9 shown ‘ Q'^2 vs Q^2 ’ distribution. The black dashed curve represent the $Q'^2 = Q^2$ line, and, red boxes represent one example bin on Q^2 , where we plan to scan over Q'^2 going from $Q'^2 < Q^2$ region to $Q'^2 > Q^2$.

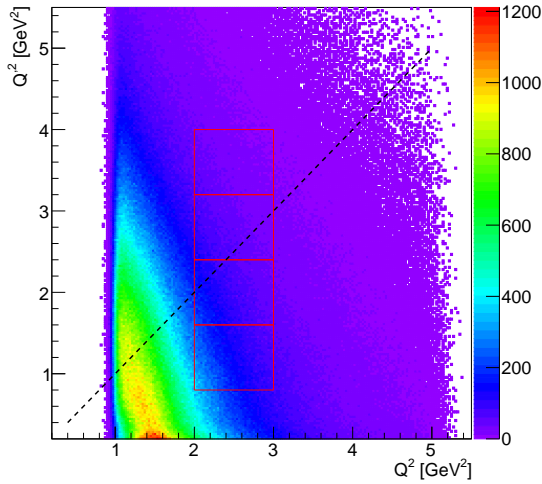


FIG. 9: “ Q'^2 vs Q^2 ” distribution. Red boxes represent an example of kinematic bins, that will be used to scan over Q'^2 , while keeping Q^2 fixed. The black dashed line represent $Q'^2 = Q^2$ line.

B. J/ψ production

The W , t , and Q^2 ranges for J/ψ production with 11 GeV electron beam with the same kinematics of scattered electron as above is shown in Figure 10. The energy range starts from the threshold and goes to little above $W = 4.5$ GeV, the reach in Q^2 and t extends to 2.5 GeV^2 .

The actual deliverables in this measurement are the following:

- Total cross section of J/ψ electroproduction

The existing data for $W > 5$ GeV support production mechanism based on 2-gluon exchange. Below W of 5 GeV, due to lack of experimental measurements and observed deviation of few measured points from 2-gluon exchange prediction, one expects possible dominance of another process for J/ψ production near threshold. The experiment E12-12-001 will measure W dependence near threshold at $Q^2 = 0$, this study will complement photoproduction results by studying the behavior of the cross section at the threshold region for different Q^2 .

- The t -dependence of the differential cross section, $d\sigma/dt$

As argued in [42], the 2-gluon form factor of the nucleon should be universal and have the dipole like dependence, $(1 - t/m_{2g}^2)^{-2}$, with $m_{2g} \approx 1$ GeV. Since there are expectations that the 2-gluon exchange mechanism is not dominant at the threshold region, study of the t -dependence, in particular dependence of the slope on Q^2 , can play an important role in understanding the scattering process.

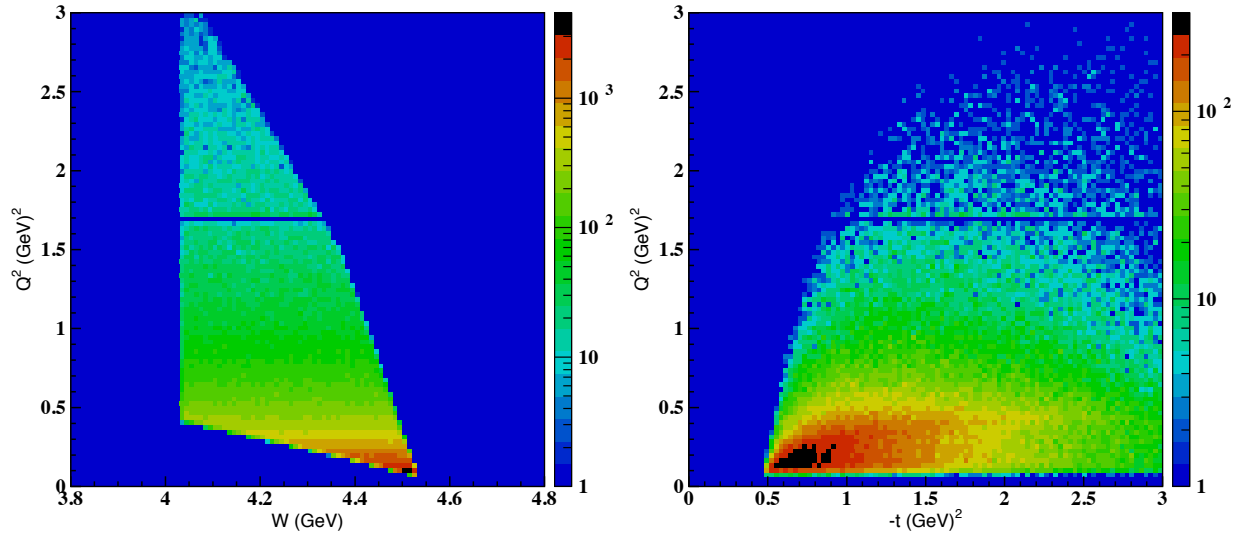


FIG. 10: Kinematics of J/ψ electroproduction with 11 GeV beam. Left, Q^2 vs. W distribution when scattered electron is detected in the polar angular range from 7° to 30° with momenta $p > 0.5$ GeV. On the right, Q^2 vs. transferred momentum squared (t) for the same selection. The slope of 1.2 GeV^{-2} for exponential t -dependence was used for J/ψ production simulations.

- Decay angular distributions and the ratio $R = \sigma_L/\sigma_T$

The angular distributions of muons in the J/ψ rest frame provide information about the photon and J/ψ polarization states. Under the assumption of SCHC [48], the normalized angular distribution can be expressed in the form

$$\frac{1}{N} \frac{dN}{d \cos \theta_h} = \frac{3}{8} \left[1 + r_{00}^{04} + (1 - 3r_{00}^{04}) \cos^2 \theta_h \right], \quad (7)$$

$$\frac{1}{N} \frac{dN}{d\psi_h} = \frac{1}{2\pi} \left[1 - \epsilon r_{1-1}^1 \cos 2\psi_h \right]. \quad (8)$$

Assuming SCHC and natural spin-parity exchange (NPE) [48], the matrix elements r_{00}^{04} and r_{1-1}^1 are related by

$$r_{1-1}^1 = \frac{1}{2} \left(1 - r_{00}^{04} \right) \quad (9)$$

and the ratio of the longitudinal to transverse cross section, $R = \sigma_L/\sigma_T$, is related to r_{00}^{04} as:

$$R = \frac{1}{\epsilon} \frac{r_{00}^{04}}{1 - r_{00}^{04}}. \quad (10)$$

In this measurements R will be studied as a function of Q^2 .

C. Search for LHCb pentaquarks

LHCb recently announced the discovery of two exotic structures in the $J/\psi + p$ decay channel, which have been referred to as charmonium-pentaquark states [49]. They labeled these states as $P_c(4380)$ and $P_c(4450)$ and claimed that the minimum quark content is $c\bar{c}uud$. The pentaquarks were observed in the decay $\Lambda_b^0 \rightarrow K^- P_c^+, P_c^+ \rightarrow J/\psi p$. One state has a mass of $4380 \pm 8 \pm 29$ MeV and a width of $205 \pm 18 \pm 86$ MeV, while the second is narrower, with a mass of $4449.8 \pm 1.7 \pm 2.5$ MeV and a width of $39 \pm 5 \pm 19$ MeV. The preferred J^P assignments are of opposite parity, with one state having spin $3/2$ and the other $5/2$.

The decays of conventional baryons to $J/\psi + X$ are strongly suppressed by the Okubo-Zweig-Iizuka rule. It provides a hint that these resonances contain a $c\bar{c}$ pair and 3 light quarks in the initial state to conserve the baryonic number. In addition, the masses of these states (≈ 4.4 GeV) are close to the sum of the mass J/ψ and proton. The narrow width (especially for the $P_c(4450)$) supports the hypothesis that these heavy baryonic states have small probability to decay to the low mass mesons and baryon, which would be very difficult to explain if these states consist of the light quarks only. So the interpretation of these structures as pentaquark with hidden charm looks very reasonable.

Since these states were observed in the decay mode $J/\psi + p$, it is natural to expect that these states can be produced in photoproduction process $\gamma^* + p \rightarrow P_c \rightarrow J/\psi + p$ where these states will appear as s-channel resonances at photon energy around 10 GeV [50–52]. In the proposed measurements they should be seen in the electron missing mass distribution (W-distribution) of events tagged with J/ψ at $W \sim 4.45$ GeV. The W-resolution and expected event rate will be sufficient to see these states if they exist.

D. Importance of the J/ψ measurements for the DDVCS studies

Since the final states for DDVCS and J/ψ are identical, the detector efficiency and resolution for exclusive J/ψ production is very similar to that of DDVCS events in the proposed range of lepton invariant mass. The narrow peak of the J/ψ will make it easy to identify the reaction and be more suitable for a reliable yield extraction than the DDVCS-BH continuum. The J/ψ electroproduction reaction can thus serve as an important benchmark, allowing us to better understand the systematic uncertainties. The $\phi(1020)$ could in principle also be used in a similar way at the lower end of the invariant mass range. A measurement of the J/ψ cross section in parallel with DDVCS will thus be very beneficial for the understanding the DDVCS data, and help addressing the two main

sources of systematic uncertainty, i.e. acceptance and the muon identification.

IV. DETECTOR CONFIGURATION

The proposed experiment requires (a) detection of muons and (b) much higher luminosity than the design luminosity of CLAS12. Occupancies in the CLAS12 forward drift chamber (FDC) are the main limiting factor for luminosity. The main source of background is Møller electrons and their secondaries. In the nominal configuration, the combination of the solenoid field (\sim few Tesla) and tungsten Møller cone, shown in the left pannel of Figure 11 in red, ensure the acceptable occupancy in FDCs at luminosity of $\sim 10^{35} \text{ cm}^{-2} \text{ sec}^{-1}$. (The tungsten cone covers region of polar angles up to 2.5 degrees and has an opening for beam to go through). Extensive simulations with a GEANT4 [53] model of CLAS12 (GEMC) [54] for optimizing the Møller cone resulted in $\leq 0.5\%$ occupancies in FDC at the nominal luminosity as can be seen on the right panel of Figure 11.

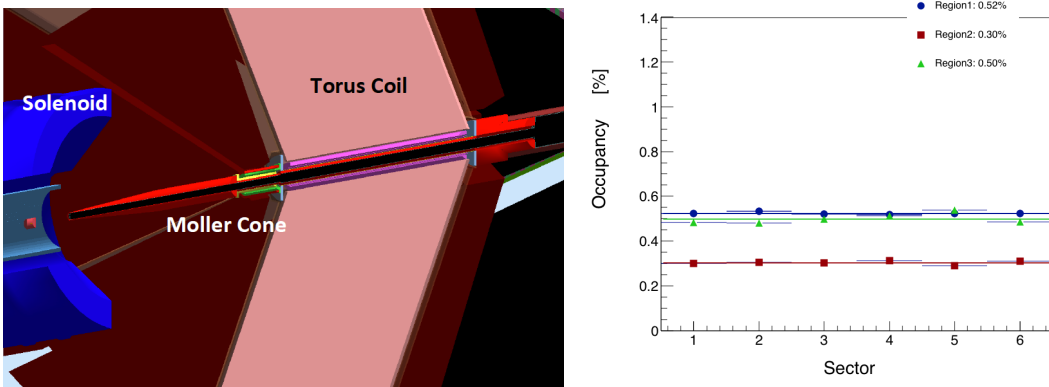


FIG. 11: Tungsten Møller cone (left) and average FDC occupancies at $\sim 10^{35} \text{ cm}^{-2} \text{ sec}^{-1}$ luminosity. Configuration without CLAS12 Forward Tagger.

This experiment aims to run with ~ 100 times higher luminosity. The detector configuration presented here is designed to provide high luminosity running capability and the detection of muons in the CLAS12 Forward Detector.

A plane view of the CLAS12 (cut in (YZ) plane) is depicted in Figure 12. As a simple solution, we propose to remove High Threshold Cherenkov Counter (HTCC) and in the region of the HTCC active volume (shown with red ellipse) install a new Møller cone that extends up to 7° in polar angle, and a new PbWO₄ calorimeter that covers 7° to 30° polar angular range with 2π azimuthal coverage. Behind the calorimeter there will be a 30 cm thick tungsten shield that covers the whole acceptance region of the CLAS12 FD. In this configuration the forward drift chambers will be

fully protected from electromagnetic and hadronic background produced in the target and able to perform at higher luminosities. In turn, this calorimeter/shield configuration, shown in Figure 13, will play a role of the absorber for the muon detector, which in this case is the CLAS12 FD. The scattered electrons will be detected in the calorimeter. There will be GEM based tracking detectors in front of the calorimeter/shield in order to aid reconstruction of vertex parameters (angles and positions) of charged particles.

We estimate the cost for the proposed modifications to CLAS12 will be $\sim \$4$ M. The PbWO₄ calorimeter will cost little below \$3 M, five GEM tracker modules \$0.8 M, and the shield and support \$0.3 M. Detector details are presented below together with detail simulations of operational conditions.

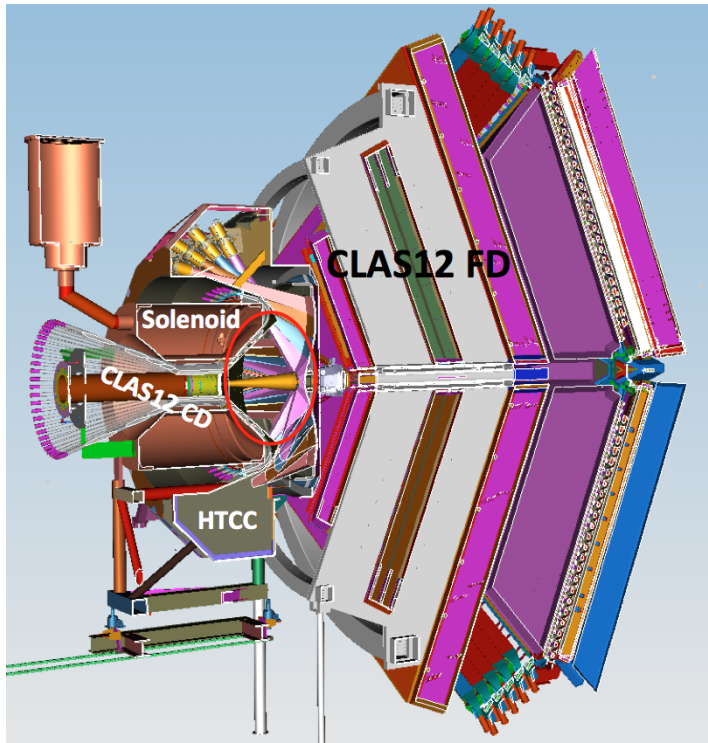


FIG. 12: The CLAS12 detector in Hall-B, mid plane cut view. The region of the working volume of HTCC is shown with red contour.

A. PbWO₄ calorimeter

The calorimeter for detection of electrons will be mounted at 60 cm from the target center and will consist of about 1200, 20 cm long PbWO₄ modules. We intend to use tapered crystals arranged to form a hexagon with hole in the center, similar to the Inner Calorimeter (IC) of the Hall-B DVCS

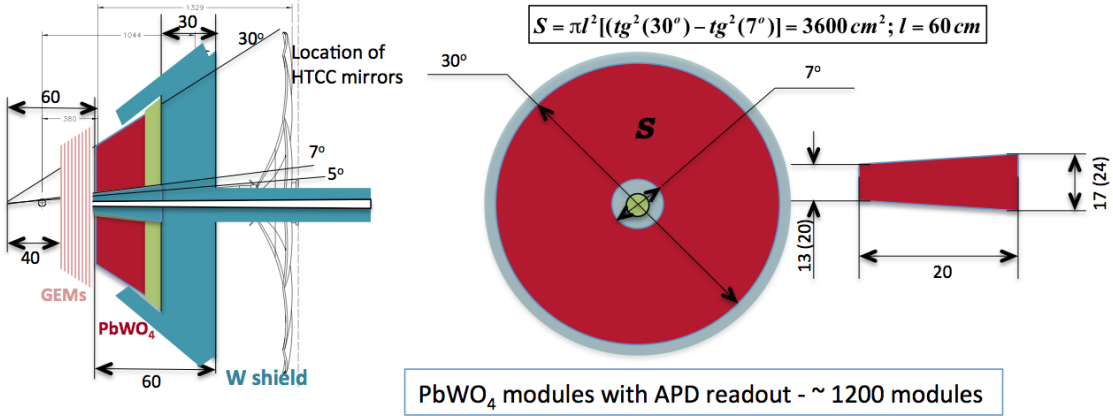


FIG. 13: The concept of the proposed shield and PbWO₄ calorimeter in the place of HTCC working gas. Dimensions on the figure are in cm, the size of PbWO₄ crystals are not optimized.

experiment [55]. The central hole will extend to 7°, the outer perimeter of the hexagon will be at 30° polar angle. In the inner part of the calorimeter, from 7° to 12° degree, the transverse size of the crystals will be 1.3 × 1.3 cm², above 12° crystals of 2 × 2 cm² will be used. The smaller size modules at forward angles are needed to keep rates per module at an acceptable level. The readout of modules will be performed with APDs from the downstream face of the crystal. Such calorimeters have been successfully used in Hall-B for 6 GeV DVCS experiment, 424 channels, Figure 14, and for Heavy Photon Search experiment (HPS), 442 channels [56], Figure 15, and one has been built for the CLAS12 Forward Tagger system, 332 channels [57], Figure 16.

The critical parameters for the calorimeter are energy and angular resolutions in high rate conditions. From two calorimeters used in Hall-B electron scattering experiments, the one for HPS operated at close to the expected conditions of this proposal. Modules for HPS calorimeter were made of tapered crystals with 1.3 × 1.3 cm² front face cross section. As photodetectors, Hamamatsu 10 × 10 mm² APDs were used. For readout and the trigger with fast clustering algorithm JLAB FADC250's were used. During the HPS production data taking, the rates in modules around the beam were ∼ 1.5 MHz, see lower panel of Figure 15. Rates of this order we expect in modules at 7° polar angle for 10³⁷ cm⁻² sec⁻¹ luminosity. The HPS calorimeter showed stable performance in two runs at 1.07 GeV and 2.3 GeV. The energy and time resolutions obtained from these data are shown in Figure 17. In the fiducial region (1 cm away from the edges) the energy resolution is 4%/√ E , the time resolution for $E > 0.4$ GeV is better than 0.5 ns.

The collaboration has extensive experience in fabricating and running PbWO₄ calorimeters. From the costbook of the last constructed one for the CLAS12 forward tagger system, the cost

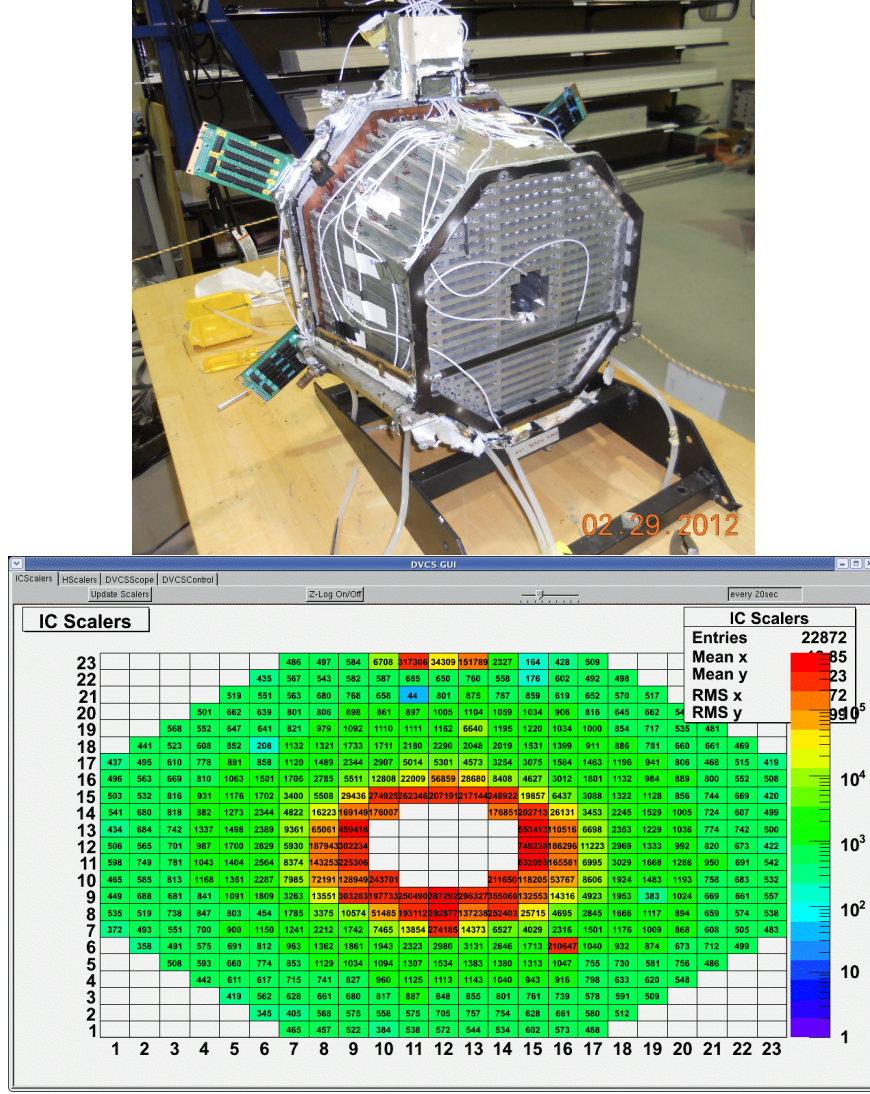


FIG. 14: CLAS Inner Calorimeter. Top - calorimeter with temperature enclosure removed.

Bottom - scaler readout in Hz for each module during one 5.7 GeV runs with LH₂ target and luminosity of $2 \times 10^{34} \text{ cm}^{-2} \text{ sec}^{-1}$ when calorimeter was at 65 cm from the target centr. Note, in the closest to the center (to the beam) modules rates are $\sim 1 \text{ MHz}$. The 7° corresponds to 6^th module from the center and rates in that modules are $\sim 2 \text{ kHz}$.

per module for PbWO₄ crystal calorimeter with APD readout averages to \$1.8K. This amounts to a total of \$2.16 M for construction of the calorimeter. Readout electronics, HV and LV power supplies, and cables are estimated to cost about \$0.75 M, bringing the total cost of the calorimeter to little below of \$3 M.

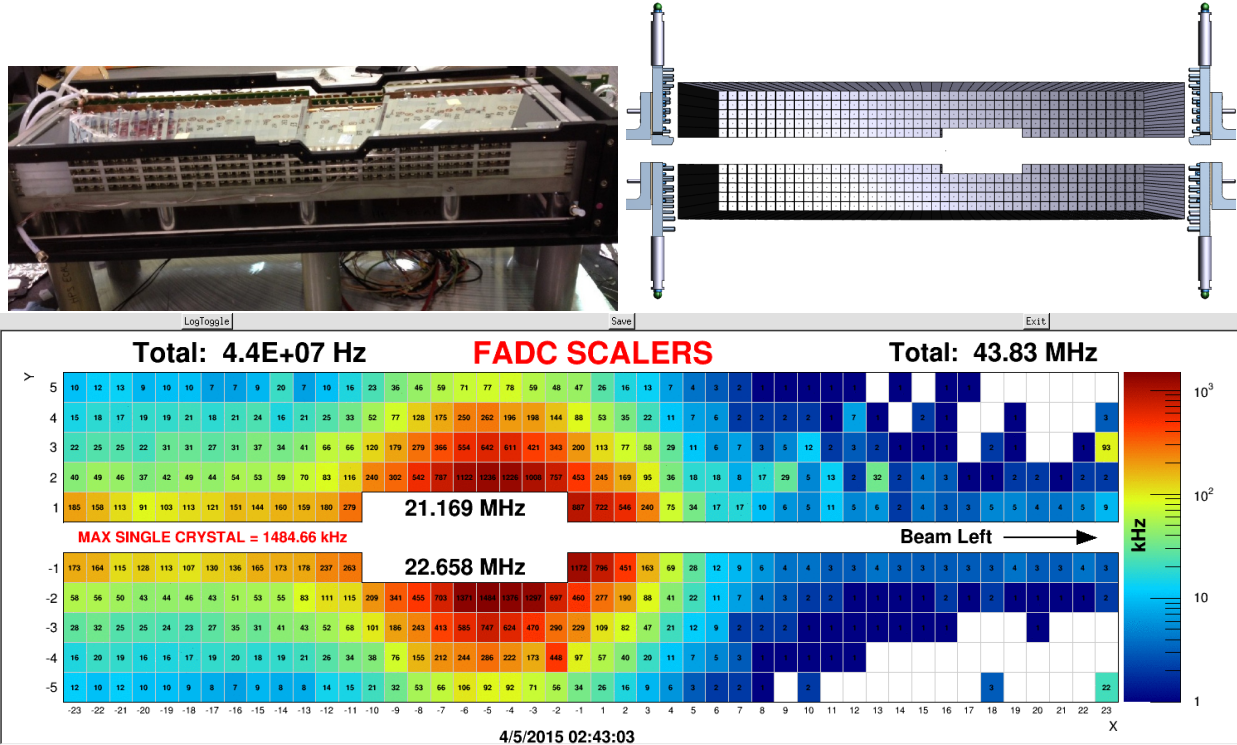


FIG. 15: HPS Calorimeter. Top - one of HPS calorimeter modules with covers removed. In the middle rendering of the module arrangement in the installed position, beam passes through middle of the large opening between top and bottom modules. Bottom panel shows snapshot of calorimeter scaler GUI during 1.07 GeV run. The highest rates in this snapshot for a single module is 1484.66 kHz.

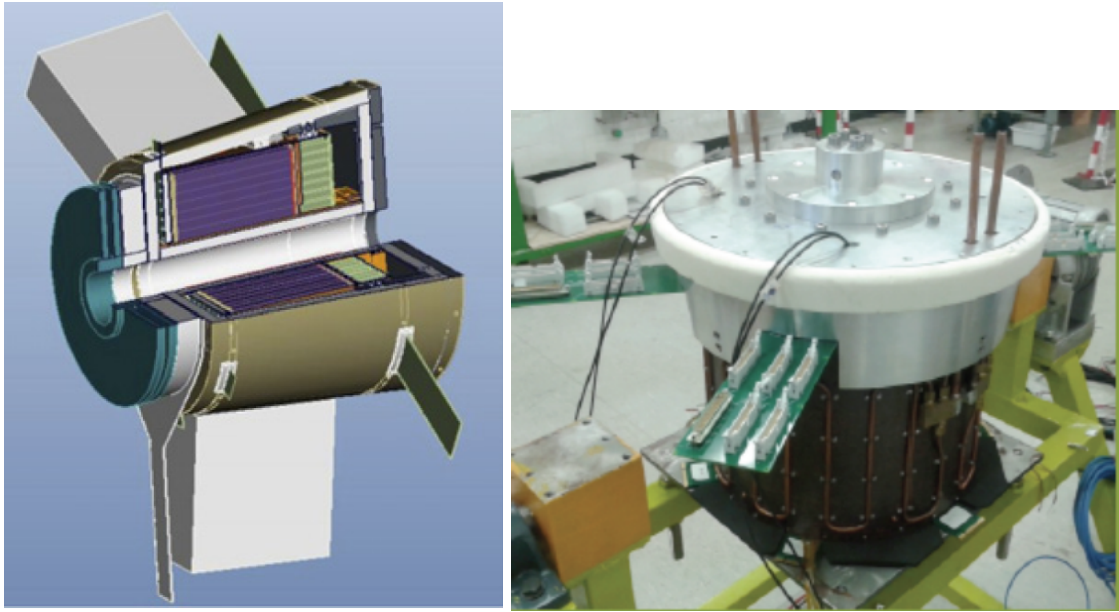


FIG. 16: CLAS12 Forward Tagger Calorimeter. Left - rendering of Forward tagger system. On the right - assembled calorimeter module.

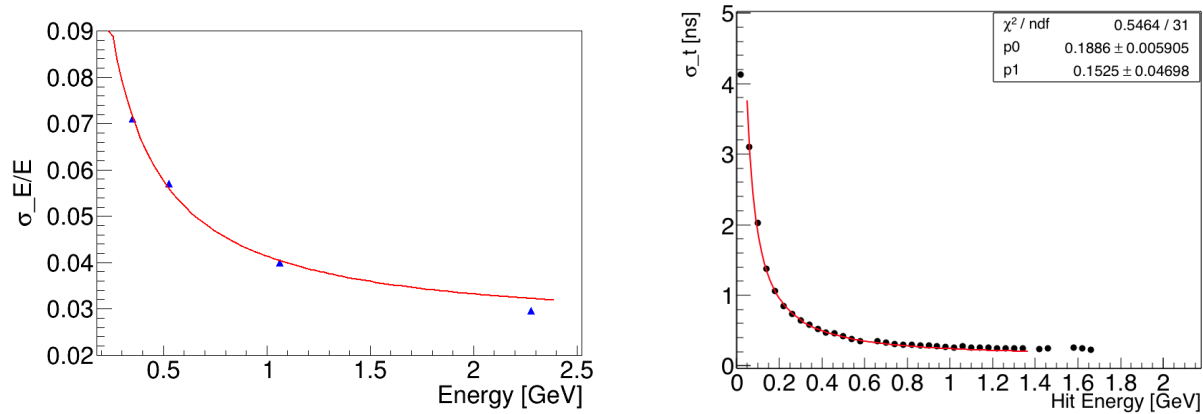


FIG. 17: Energy (left) and time (right) resolutions of HPS calorimeter as a function of electron energy.

B. GEM tracker

Proposed experiment requires detection of three charged particles, e^- in the calorimeter, and $\mu^+\mu^-$ in the CLAS12 Forward Detector. All three will emerge from the target and go through a high magnetic field (CLAS12 solenoid) before getting into detectors. In addition, muon pairs have to pass through calorimeter material and tungsten shield before getting momentum analyzed. These conditions will not allow to define track vertex parameters (production vertex point and production angles) with required accuracy using only information from outer detectors. As in CLAS12, there will be a need for a tracking detector close to the target to aid charge particle vertex parameter determination.

For the tracking detector we choose GEM technology. The GEM is based on gas avalanche multiplication within small holes (on a scale of $100\ \mu\text{m}$), etched in a Kapton foil with a thin layer of copper on both sides. The avalanche is confined in the hole resulting in fast (about 10 ns rise time) signals. Several GEM foils (amplification stages) can be cascaded to achieve high gain and stability in operation. The relatively small transparency of GEM foils reduces the occurrence of secondary avalanches in cascaded GEM chambers. All these properties result in very high rate capabilities of up to 100 MHz per cm^2 and an excellent position resolution of $70\ \mu\text{m}$. Fig. 19 illustrates the principle of operation of a triple (three foil) GEM chamber.

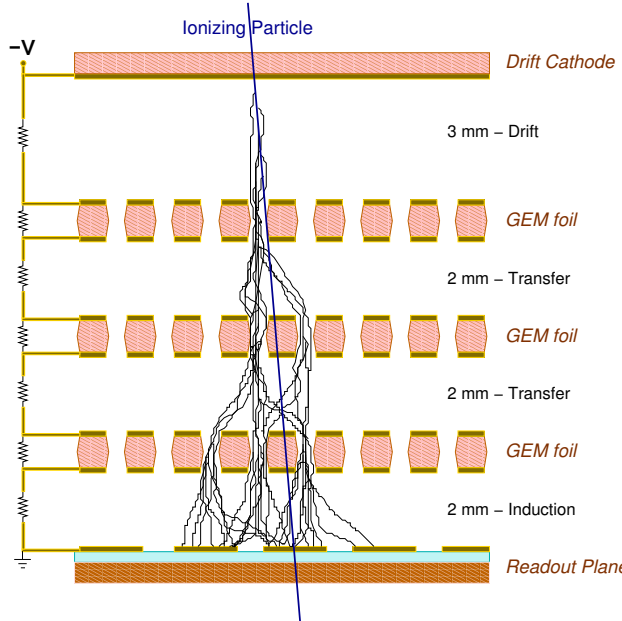


FIG. 18: Principle of triple GEM operation.

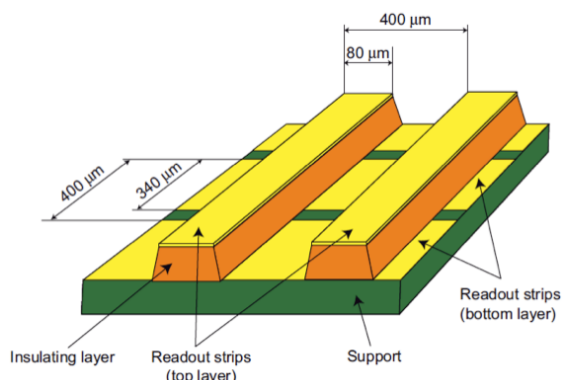


FIG. 19: 3D view of the readout board.

GEM based tracking detectors have been used in several JLAB experiments, e.g. Hall-B Bonus [58], eg6 ^4He [59], and Proton Charge Radius [60] experiments. High rate GEM trackers that can handle up to 1 MHz/cm² rates are currently being fabricated for Hall-A SBS [61] spectrometer, and are prototyped for the proposed SoLid [62] device. In the case of SBS and SoLID, the rate limitation arises due to occupancy rates on relatively long (~ 70 - 120 cm) readout strips and not due to any intrinsic rate limitation in the GEM detector itself.

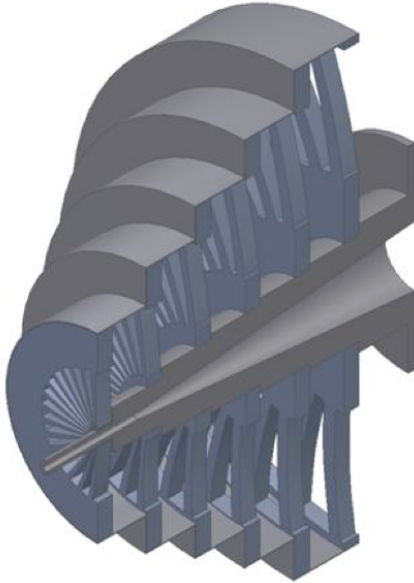


FIG. 20: Five GEM trackers (left) and 2D readout pads (right).

We propose to use "disk" design for the tracking chambers, similar to SoLid GEM tracker design but in much smaller scale. There will be five tracking detectors installed between target and the calorimeter as shown on left panel of Figure 20. The first detector will be at 40 cm from the target. Tracker will cover angular range from 5° to 35° . Each disc will be divided azimuthally into six trapezoidal sections to match six-fold symmetry of CLAS12. In the present conceptual a trapezoidal GEM section in each disc will have an inner radius of 3.5 cm and an outer radius of 42 cm, with an inner width of 4 cm and outer width of 44 cm. The readout will be done using 2D readout strips, with radial and ϕ -readout strips to define polar and azimuthal angles. The average length of a radial readout strips at smallest angles ($\sim 5^\circ$) in each sector is 4.5 cm. Given the relatively short length of readout strips required for these detectors and using simulations and prototyping of GEM detectors for SBS and SoLid, the proposed tracker can run at rates of 2.5 MHz/cm² and will have position resolution better than 100 μm [63].

Two members of our collaboration from University of Virginia are well recognized experts in the field and are leading prototyping and construction of GEM trackers for SBS and SoLid. The proposed detector for this experiment does not pose any challenges in terms of operational conditions or size. Most of R&D for such detectors are already done or close to be complete. The whole construction effort for five modules has been estimated to be $\sim \$0.8$ M.

C. Background studies and luminosity limits

Detailed simulations of background rates and detector occupancies for the proposed configuration have been carried out using the same CLAS12 simulation software, GEMC, that was used to optimize the Møller shield for the nominal configuration. The GEMC model of the detector is shown in Figure 21. The thicknesses and coverage of the calorimeter/shield configuration were optimized after detailed studies of the drift chamber occupancies, which are the limiting factor for CLAS12 luminosity. The same simulations have been used to estimate hadronic background and trigger rates using the GEANT4 physics model described in [64].

The studies were done at 10^{35} cm $^{-2}$ sec $^{-1}$ luminosity using a 5 cm long liquid hydrogen target with events in the time window of 252 ns, grouped in bunches of 4 ns. That corresponds to $\sim 120,000$ incident electron events, with 1898 e $^-$ per bunch for each of the 63 bunches. The rates provided below were obtained by simply multiplying numbers from the simulation by $\times 100$.

1. Occupances in Forward DCs

Several different thicknesses of shield have been studied, and the one described above had the optimum performance. In Figure 22 average occupancies of Region 1 and 2 DC are shown for different absorber thicknesses after scaling rates by $\times 100$ for luminosity of 10^{37} cm $^{-2}$ sec $^{-1}$. As can be seen, for absorber thicknesses above 20 cm occupancies in Regions 1 and 2 FDC stay almost constant. The final thickness of the absorber was chosen to be 30 cm based on considerations of π/μ separation, muon energy loss, and the muon momentum resolution (see below). In Figure 22, right panel, occupancies of all three regions of drift chambers are shown for final configuration. The highest occupancy is in Region 3, $\sim 3.5\%$ (after discarding the 16 shortest wires closest to the beam). Occupancies in Regions 1 and 2 are $< 2\%$. The source of the difference between occupancies of Regions 1 and 2, and Region 3 is well understood: the scattered beam interacts with the downstream end of the torus hub producing secondary electromagnetic background.

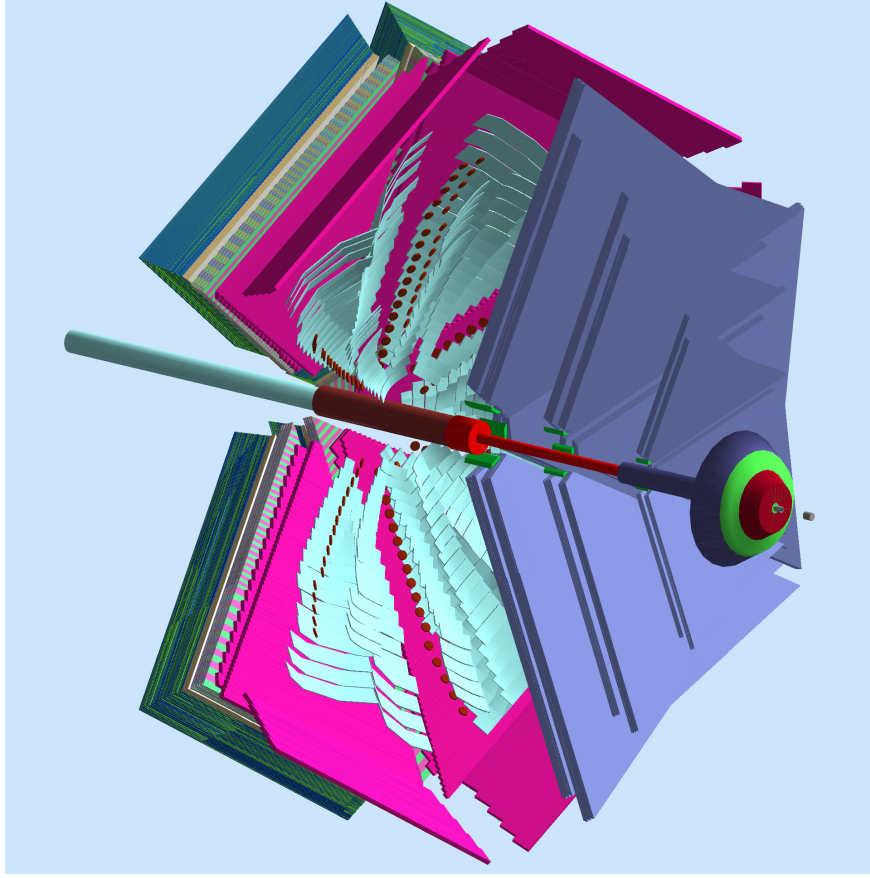


FIG. 21: The forward part of the modified CLAS12 detector. The dark blue is the tungsten shield with Møller cone. Dark red is the calorimeter, with space for readout shown in light green.

2. Rates in GEM tracker

In order to estimate rates in the GEM tracker a scoring plane was introduced in the GEANT4 model at 40 cm from the target center. Any particle that passes the plane between 4.8° and 35° angular range was counted as a hit. In Figure 23 the rates of pions, protons, electrons, and photons from interaction of 11 GeV electron beam with LH₂ target at the luminosity of $10^{37} \text{ cm}^{-2}\text{sec}^{-1}$ are presented as MHz per cm². The highest rate is from photons (energy cut in GEANT was > 10 keV). From separate studies of GEM detectors performed for SoLid and SBS, it is known that only 0.5% of photons with $E > 10$ keV will leave detectable signal in the tracker. With this factor, the total integrated rate in the GEM tracker at $\sim 5^\circ$ will be < 0.6 MHz/cm². The length of the radial readout in our design presented above is 4.6 cm and area of coverage, with 400 μm pitch size, is 0.18 cm². So we expect ~ 0.1 MHz average rate for the hottest strips. This rate is very much within the limits of operation of the GEM tracker.

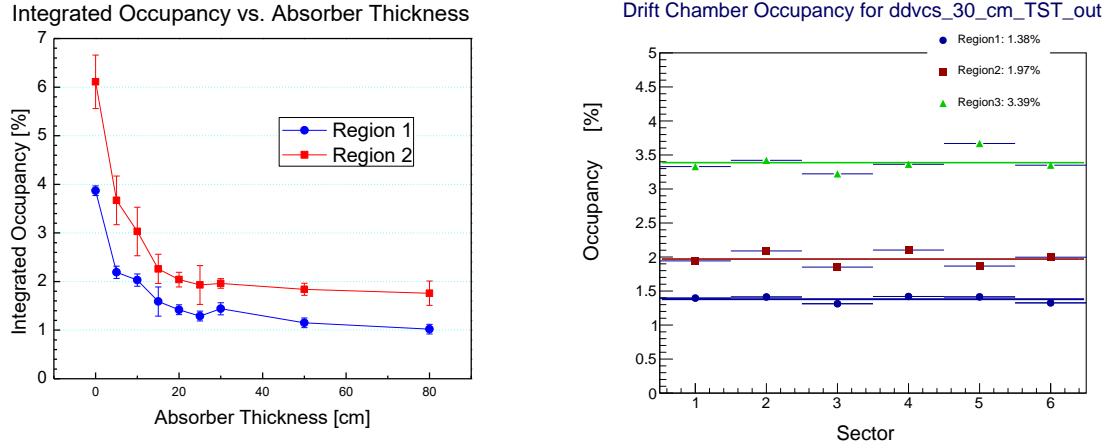


FIG. 22: On the left: CLAS12 FDC Region 1 and 2 average occupancies for different absorber thicknesses behind the calorimeter. On the right: FDC average occupancies at luminosity of $10^{35} \text{ cm}^{-2} \text{s}^{-1}$

3. Rates in PbWO_4 calorimeter

In order to estimate rates in the calorimeter, the whole volume was divided into $1.3 \times 1.3 \times 20 \text{ cm}^3$ rectangles, modules. Hit in the module was counted if the energy deposition in the PbWO_4 crystal exceeded the threshold energy of 15 MeV. In Figure 24, rates in individual modules at luminosity of $10^{37} \text{ cm}^{-2} \text{sec}^{-1}$ are presented for pions, protons, electrons and photons. The inner modules start at 7° , the outermost modules are at 30° degree. Again, the highest rates are from photons, for innermost modules it reaches $\sim 2 \text{ MHz}$. The integrated rates from pions, protons and electrons for innermost modules is $\sim 0.7 \text{ MHz}$. The total rate in the "hottest" modules then will be $< 3 \text{ MHz}$, which is manageable considering that readout with FADCs will allow to handle pileup.

D. Muon identification and trigger rates

Muons will punch through the calorimeter/shield and be detected in CLAS12 FD, Figure 25. They will be identified as charged tracks in Forward DCs with the signature of a minimum ionizing particle in the Forward Electromagnetic Calorimeter (PCAL/EC-Inner/EC-Outer). Some hadrons, mostly pions, will punch through the shield and can leave similar signature in forward detectors. GEANT4 simulations have been used to study pion background in the muon sample and contribution to the trigger rates. The background rates have been estimated based on 50000

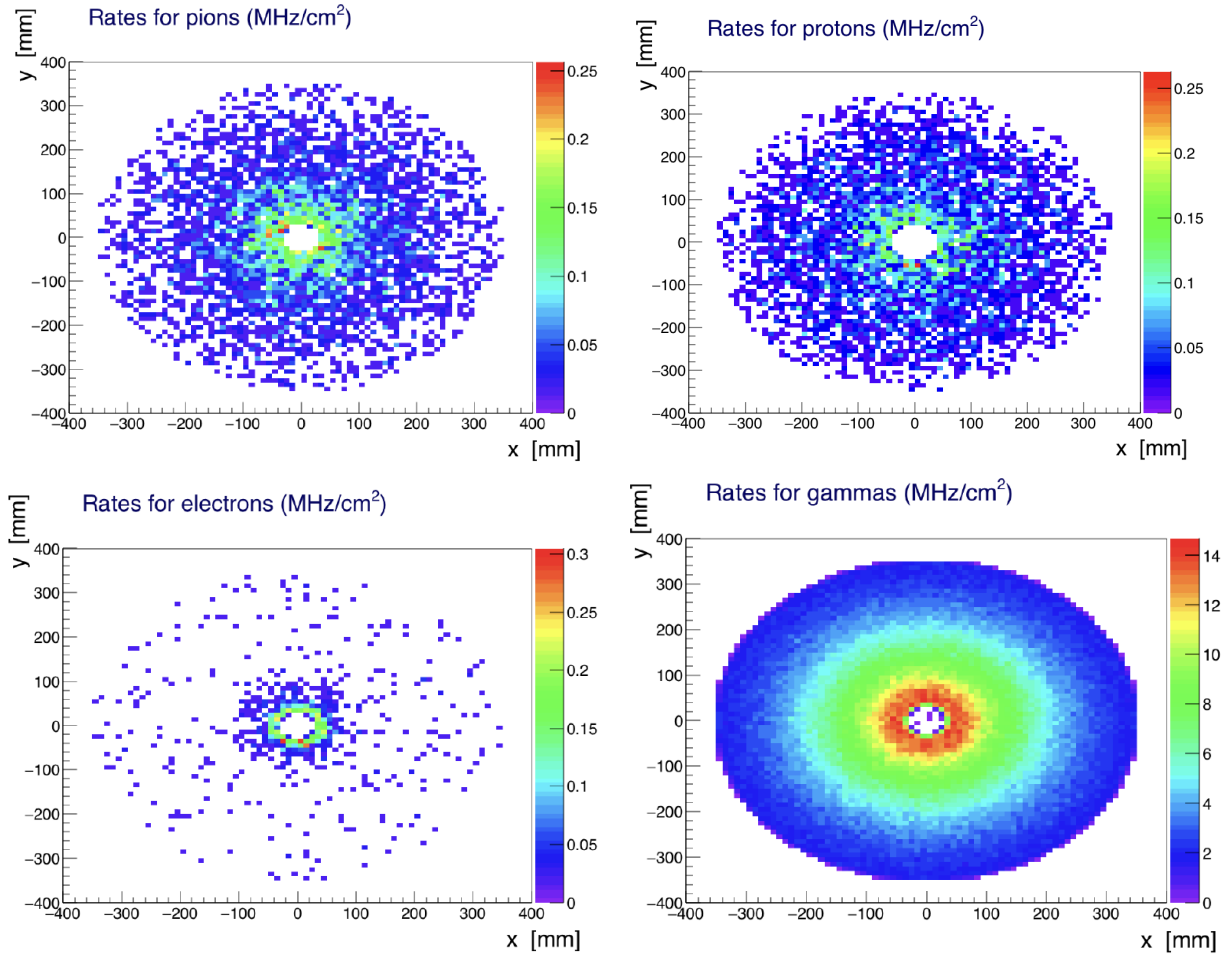


FIG. 23: Rates of pions, protons, electrons and photons on a scoring plane at 40 cm from the target, where GEM tracker starts, from 4.8° to 35° .

simulated electron scattering events.

1. Trigger rates

The rates of single charged tracks from background processes that will be detected in at least 5 out of 6 layers of FDC at luminosity of 10^{37} cm⁻²sec⁻¹, were found to be ~ 150 kHz and ~ 190 kHz for positively and negatively charged tracks, respectively. The MIP energy cut in Forward EC rejects more than 50% of these tracks, bringing singles rate to $\sim 75/95$ kHz. With trigger time window of 50 ns, the accidental coincidence rate of pairs of oppositely charged tracks with MIP energy in FEC will be ~ 360 Hz. The rate of true muon pairs, mostly from the Bethe-Heitler process, was estimated using GRAPE event generator [65] to be ~ 1 Hz. So the trigger for the

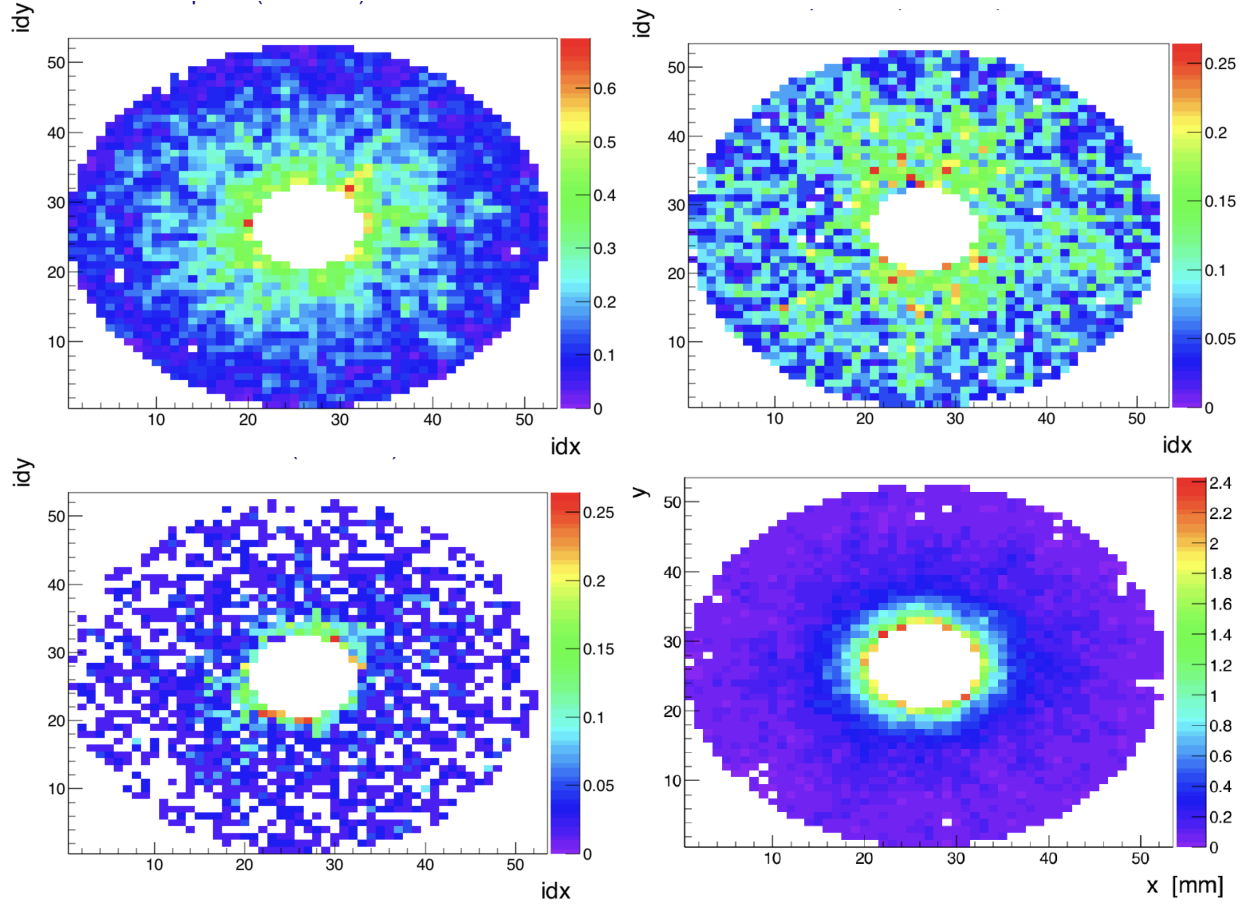


FIG. 24: Rates of pions (top-left), protons (top-right), electrons (bottom-left) and photons (bottom-right) in the calorimeter modules with 15 MeV threshold.

experiment can be two oppositely charged tracks in CLAS12 FDC with MIP energy deposition in the forward calorimeter.

2. Identification of $e^- \mu^+ \mu^-$ and accidental background

In offline analysis the $(e^- \mu^+ \mu^-)$ final state will be identified as two oppositely charged MIP in CLAS12 FD paired with "electron" like hit in the PbWO₄ calorimeter.

As an electron, clusters with energy > 0.4 GeV that have negatively charged GEM track pointing to it will be selected. From simulation we found that rate of non-electrons with that signature (all π^- s) is 0.84 MHz. Kinematic cuts to select "electrons" in the region of interest in W and Q^2 reduces this rate to 150 kHz. The true (inclusive) electron rates have been estimated using parametrization of electron scattering inclusive cross section from [66], and was found to be ~ 650 kHz. So the total rate of clusters with more than 0.4 GeV energy in the calorimeter will be 800 kHz.

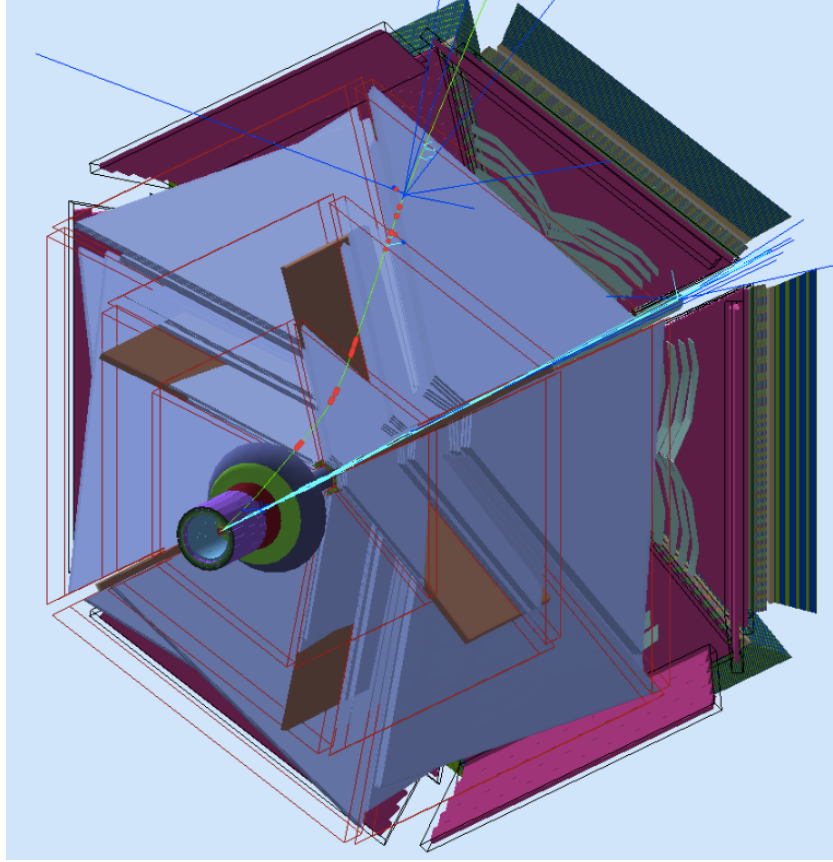


FIG. 25: A $3 \text{ GeV}/c \mu^+$ generated at a polar angle of 10° as detected in CLAS12, accompanied by 1000 beam electrons impinging the hydrogen target.

The background rates in CLAS12 FD can be improved with two factors, first using GEM tracker to select particles that come from the target region. This will give 60% reduction, bringing singles rates down to 30/40 kHz for positively/negatively charged tracks. Then tight timing cut can be applied to select pairs coming from the same beam bucket. The time resolutions of the CLAS12 FTOF and FEC are good enough to do this selection. The rate of "muon" like accidental pairs after these two additional cuts is found to be $\sim 5 \text{ Hz}$ (statistical error on this number is $\sim 30\%$ due to limited number of GEANT simulated events). Additional cuts can be applied on pair invariant mass since we are interested in masses $> 1 \text{ GeV}$. That will reduce accidental coincidence rate by another $\times 2$, see Figure 26. The rate of true muon pair rate with $M_{\mu\mu} > 1 \text{ GeV}$ cut will be 0.6 Hz, see Figure 27.

Finally, combining the rate of "electrons" in the calorimeter, 800 kHz, and the rate of muon and muon-like pairs in CLAS12 FD, 3.1 Hz, and the time window of 4 ns (beam bunch separation), one gets 0.01 Hz for accidental background rate in $e^- \mu^+ \mu^-$ sample. Another kinematic selection

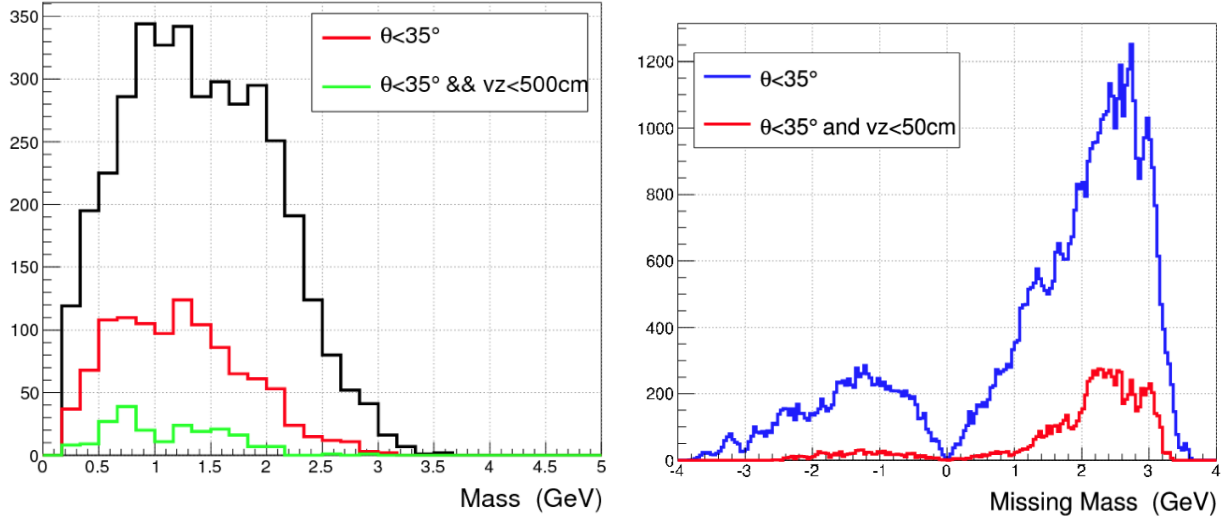


FIG. 26: Left: the invariant mass of accidental coincidence tracks in CLAS12 FD. Right: the missing mass distribution of accidental hit in the calorimeter and two oppositely charged tracks in CLAS12 FD.

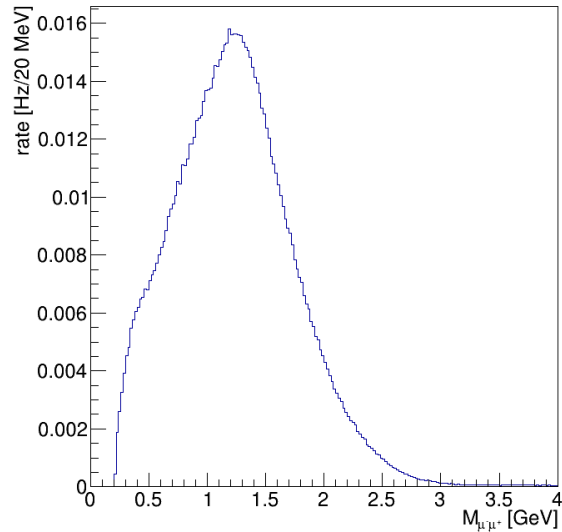


FIG. 27: Invariant mass of muon pairs detected in CLAS12 from Bethe-Heitler process.

that will reduce this rate by $\times 3$ is the missing mass of accidental (fake) $e^- \mu^+ \mu^-$ final state. For real physics events the missing mass should be the proton mass (within detector resolution). As shown in the right panel of Figure 26, only 1/3rd of events are in the range from 0 to 2 GeV. This brings accidental or "fake" $e^- \mu^+ \mu^-$ rates down, less than 0.004 Hz. For comparison, the true

Bethe-Heitler event rate with $Q^2 > 1.5 \text{ GeV}^2$, $W > 2 \text{ GeV}$ and $M_{\mu\mu} > 1 \text{ GeV}$ is 0.02 Hz.

3. Muon energy loss and momentum resolution

Muons will lose about 1 GeV energy in the calorimeter/shield before getting into the forward tracking region, see top-left panel of Figure 28. Parametrization of momentum loss, as well as fluctuations of that loss (top-right pannel of the figure) as a function of true momentum of the muon have been used to apply energy loss during event simulation in CLAS12 Fast MC for acceptance and resolution studies. After fiducial acceptance cuts, and momentum and angle smearing in CLAS12, energy loss correction was applied using parametrization of the momentum loss as a function of reconstructed momentum (bottom-left panel of Figure 28). The resulting momentum resolution is shown in the bottom-right panel of the figure. The effect of this additional smearing on the invariant and missing mass reconstruction will be discussed below.

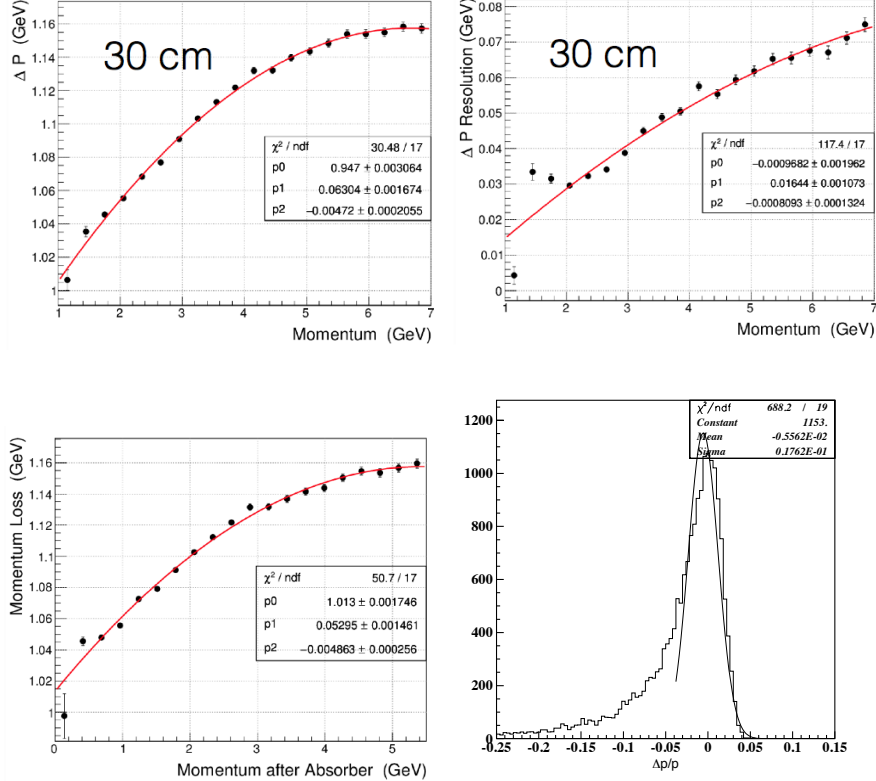


FIG. 28: Muon energy loss in the calorimeter + 30 cm absorber. Top left, momentum loss as a function of true momentum, top right momentum loss spread, standard deviation, as function of true momentum, bottom left momentum loss as a function of reconstructed momentum, and bottom right momentum resolution after energy loss correction.

E. Beam and Target

Experiment will use the standard Hall-B beam line with few modifications to support high current beam transport. We will use Hall-B liquid hydrogen target positioned at the center of the solenoid magnet. The target cell will be ~ 20 cm long. This is somewhat longer than what has been used for the CLAS electroproduction experiments in the past, but this should not be a problem for the Hall-B target system, which is capable of supporting such long cells (photon experiments in Hall-B used 40 cm long 4 cm in diameter cells). In order to achieve luminosities needed for this experiment, $\sim 10^{37}$ cm $^{-2}$ sec $^{-1}$, beam currents of ~ 2 μ A will be needed. The energy deposition in the target from 2 μ A, 11 GeV electron beam will be ~ 14 W. This heat load, while very modest for high power targets operated at JLAB, is close to the limit of the heat exchanger of the Hall-B/Saclay target. Some studies may be needed to make sure target will work.

The Hall-B electron beam dump will need modifications to handle beam power of 22 kW from 11 GeV, 2 μ A beam (existing beam dump can support up to 5 kW power, which is ~ 450 nA at 11 GeV). The rest of the beamline control and diagnostic elements will work with high current beam.

In order to limit radiation to the Central Time-of-Flight and Central neutron detectors (that most likely will remain in the solenoid magnet), we intend to surround the target cell with a lead cylinder.

V. CROSS SECTIONS, PRODUCTION RATES, AND EXPECTED PHYSICS RESULTS

A. DDVCS Cross Section and Expected Rates

Full Monte-Carlo has been performed for the reaction $ep \rightarrow e'\mu^-\mu^+p$ in order to calculate acceptance and expected rates. The VGG code [67] that calculates the DDVCS cross sections is relatively slow (around 1 second per event), and is not very practical for generating millions of events. Since in most of the kinematics BH cross-section dominate over the DDVCS and the interference terms, for the purpose of the estimation of the count rates and understanding the detector resolutions, we used the GRAPE-dilepton event generator [65], which supports BH reaction and is very fast. The incoming beam energy is assumed to be 11 GeV .

Simulations were limited in the $Q^2 \in (1 - 5) GeV^2$ region. Generated BH events were passed through the CLAS12 FastMC package (described in a previous section). In Figure 29 distributions of some kinematic variables are shown: In the top left panel generated Q'^2 vs Q^2 , and in the top right reconstructed distributions. Bottom row represent $-t$ vs x_B distributions for two different kinematic bins, when $Q^2 \in (2-3) GeV^2$ and $Q'^2 \in (0.8-1.6) GeV^2$ (left) and $Q'^2 \in (2.4-3.2) GeV^2$ (right).

In this LOI we will present estimated rates and statistical uncertainties of beam spin asymmetries as a function of Φ_L (the angle between electron scattering plane and hadronic plane) by fixing kinematic bin $Q^2 \in (2. - 3.) GeV^2$, $-t \in (0.1 - 0.4) GeV^2$, $x_B \in (0.12 - 0.22)$ (See bottom row of Fig.29), and varying $Q'^2 = 1.2, 2, 2.8, 3.6 GeV^2$. The angle Φ_L and other DDVCS relevant angles are described in Fig.30

Kinematic distributions of final state particles, when e^- , μ^- and μ^+ are detected, are shown in Fig.31, where (a), (b), and (c) represent "θ vs P" distributions for μ^- , μ^+ and e^- respectively, and (d) is the missing mass of detected $e^-\mu^-\mu^+$ system. The missing mass resolution is good enough to ensure exclusivity of the reaction.

For the aforementioned kinematic bin, the acceptance and expected rates in four bins of Q'^2 are shown in Fig.32. As one can see the acceptance is 3% to 6%. Later to estimate statistical uncertainties on the Beam Spin asymmetries, each Q'^2 bin is divided into 12 bins in Φ_L , and for each bin counts and statistical error-bars on asymmetry as a function of Φ_L are shown in Figs. 33, 34, 35 and 36. These estimations were performed assuming $10^{37} cm^{-2}s^{-1}$ luminosity and 100 days of running.

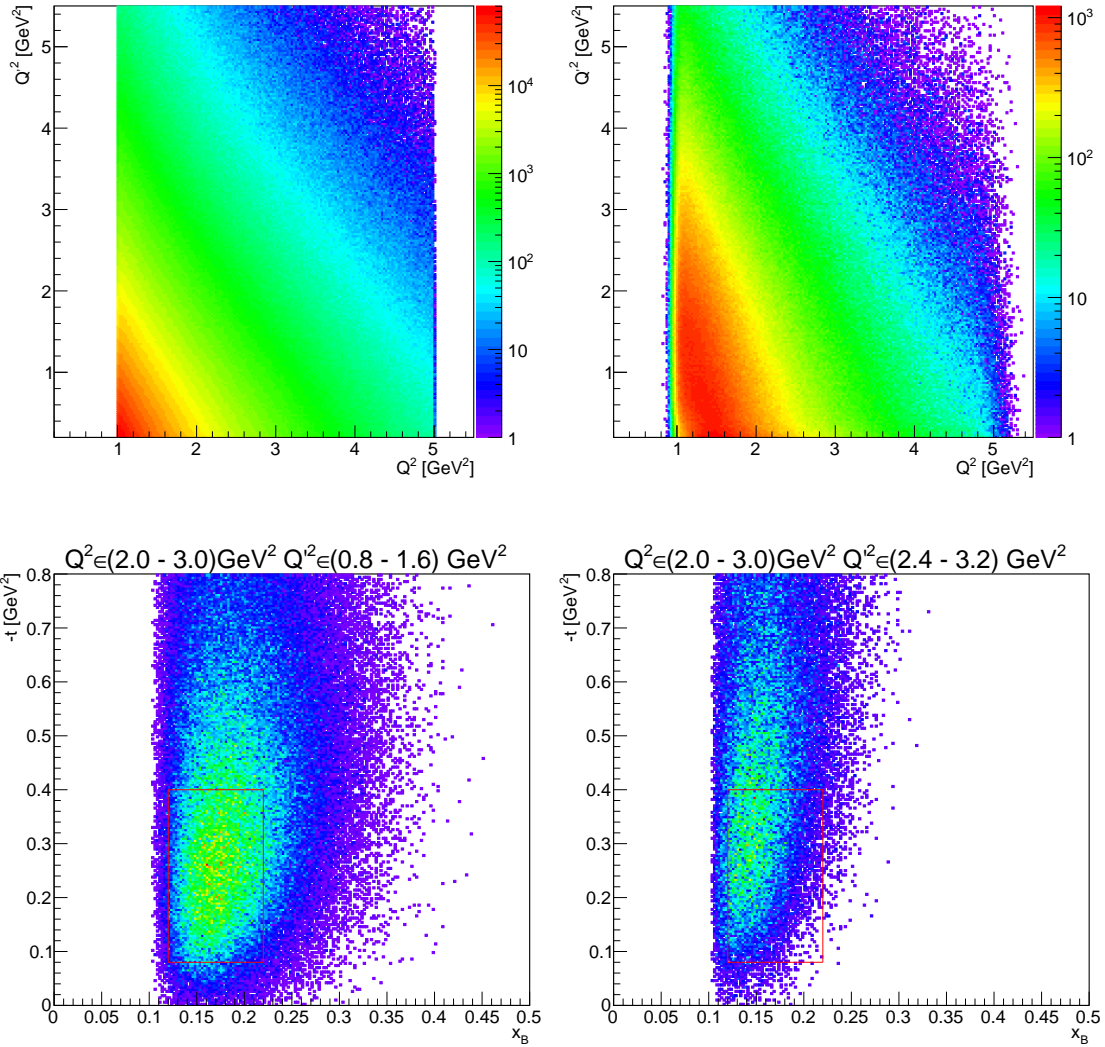


FIG. 29: Top row: Generated (left) and reconstructed (right) distributions of Q'^2 vs Q^2 . Bottom row: reconstructed "– t vs x_B " distributions, when $Q^2 \in (2.0 - 3.0) \text{ GeV}^2$ and $Q'^2 \in (0.8 - 1.6) \text{ GeV}^2$ (left) and $Q'^2 \in (2.4 - 3.2) \text{ GeV}^2$ (right).

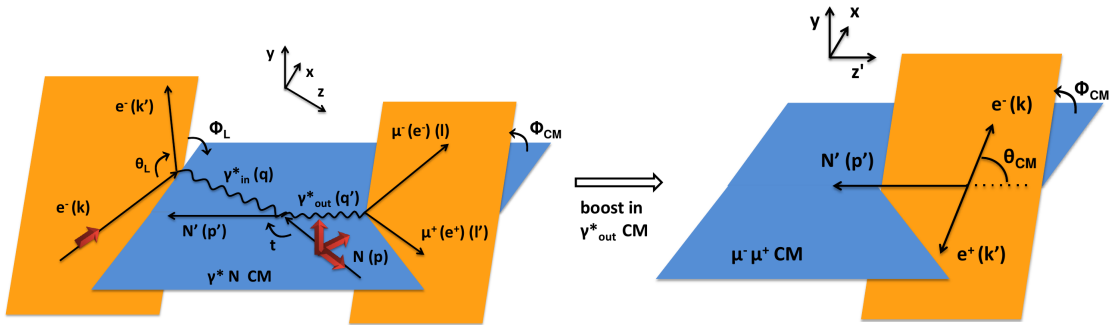


FIG. 30: Representation of DDVCS angles. Φ_L is the angle between beam scattering and hadronic planes (left figure), Φ_{CM} is the angle between decay lepton and hadronic planes (left figure) and Θ_{CM} (right figure) is the angle of the negative decay lepton w.r.t. scattered proton momentum, in the frame where timelike photon is at rest.

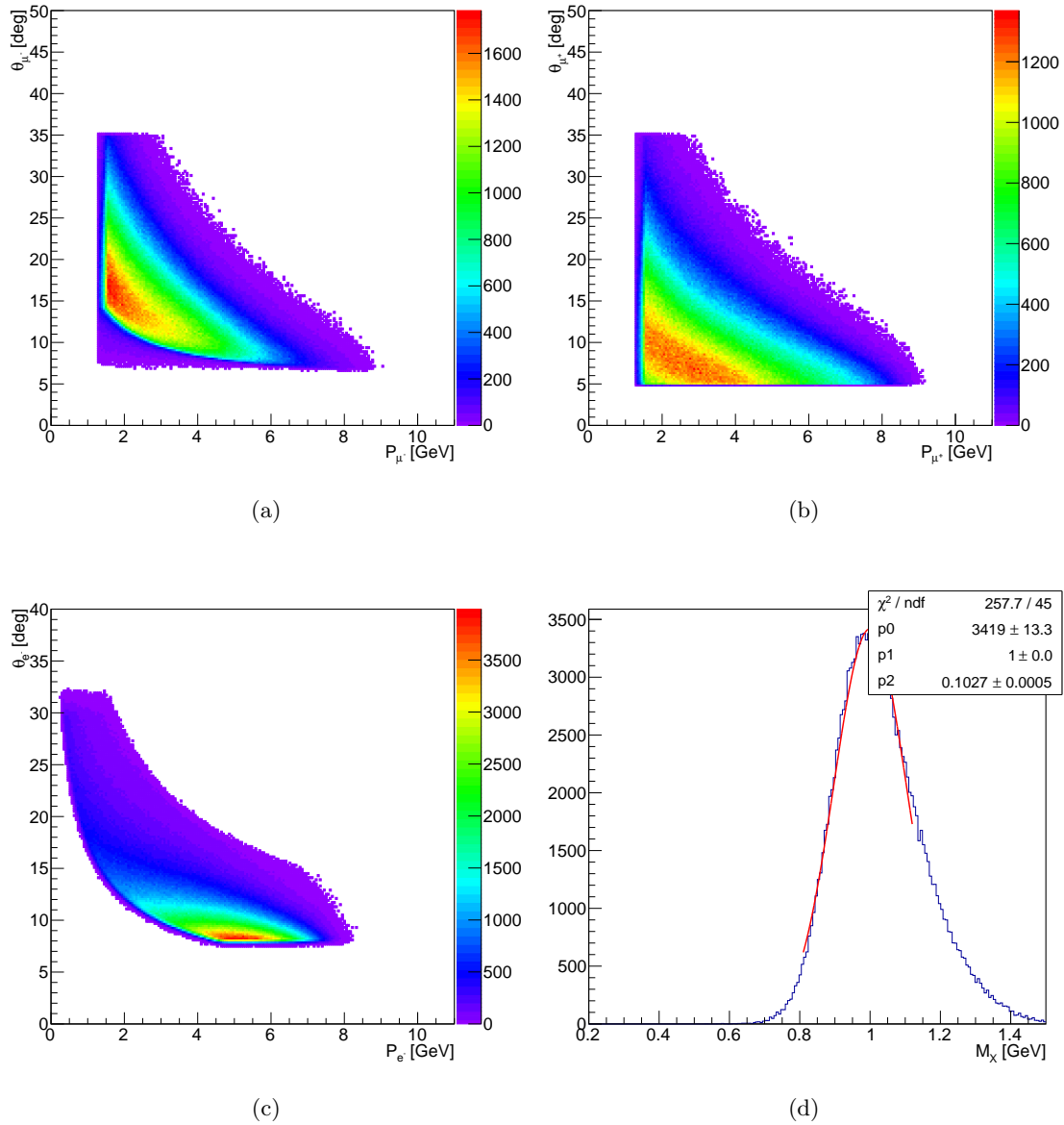


FIG. 31: θ vs P distributions for detected μ^- (a), μ^+ (b) and e^- (c). (d) is the missing mass of detected $e^- \mu^- \mu^+$ system.

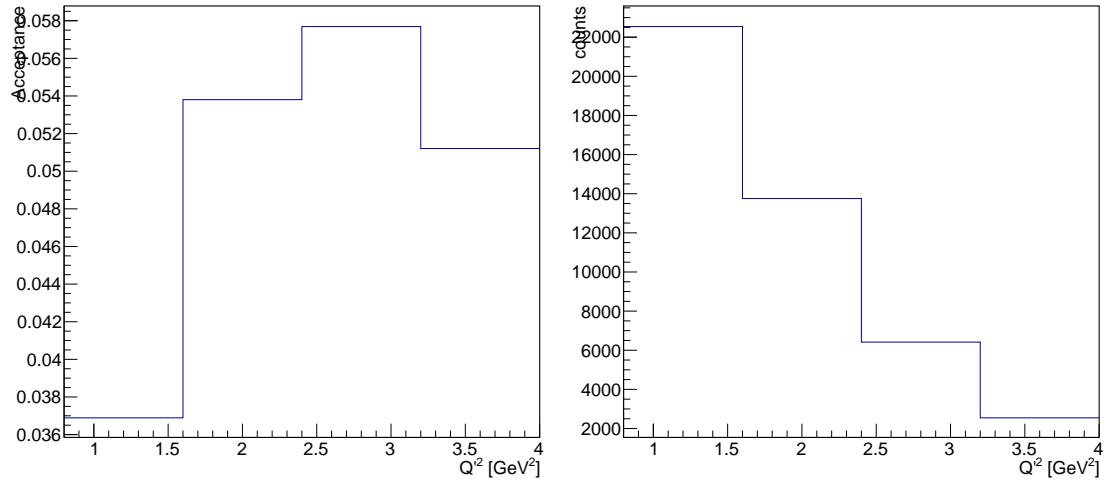


FIG. 32: Acceptance (left) and expected rates (right) for different bins of Q'^2 .

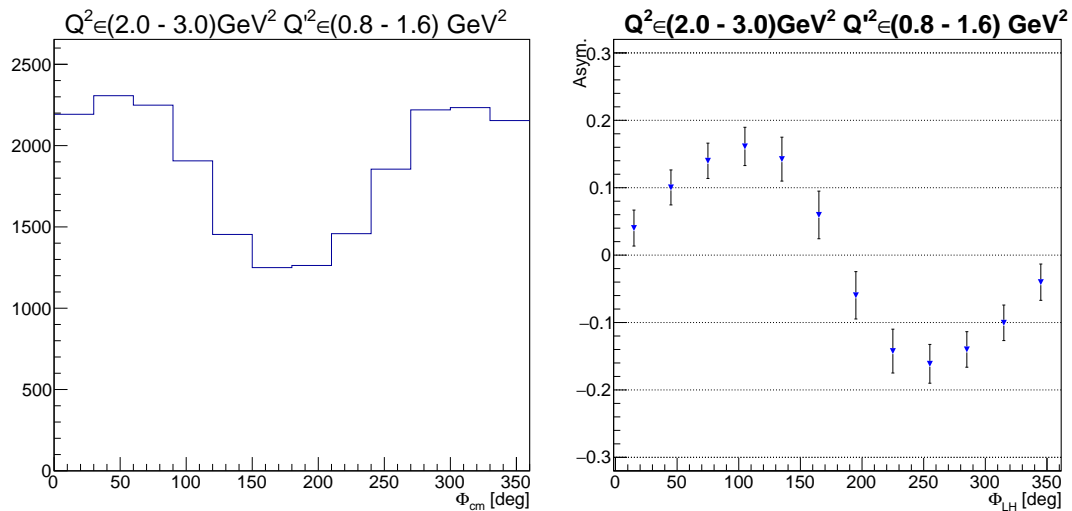


FIG. 33: Count rates (left) and statistic error-bars (right) for the $Q'^2(0.8 - 1.6) \text{ GeV}^2$ bin.

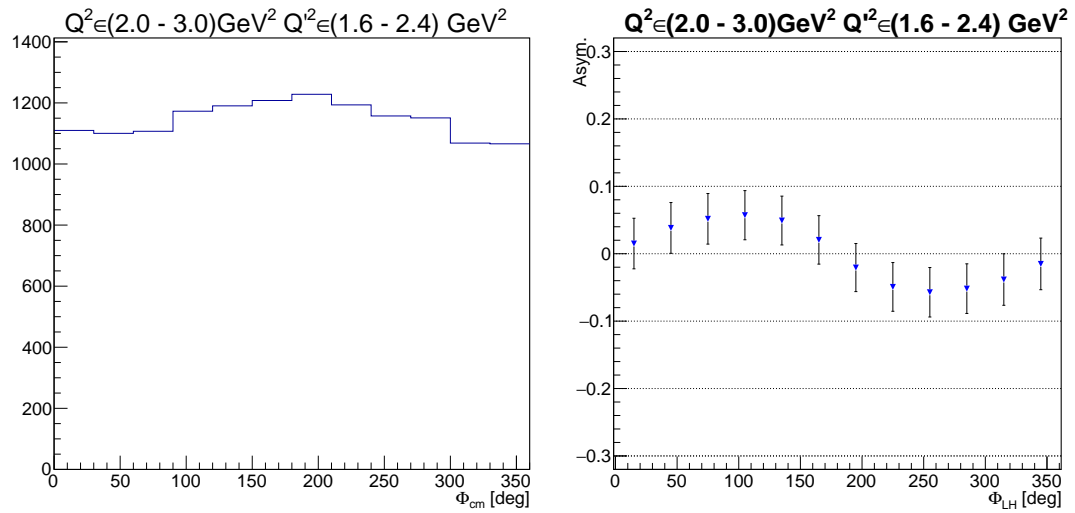


FIG. 34: Count rates (left) and statistic error-bars (right) for the $Q'^2(1.6 – 2.4) \text{ GeV}^2$ bin.

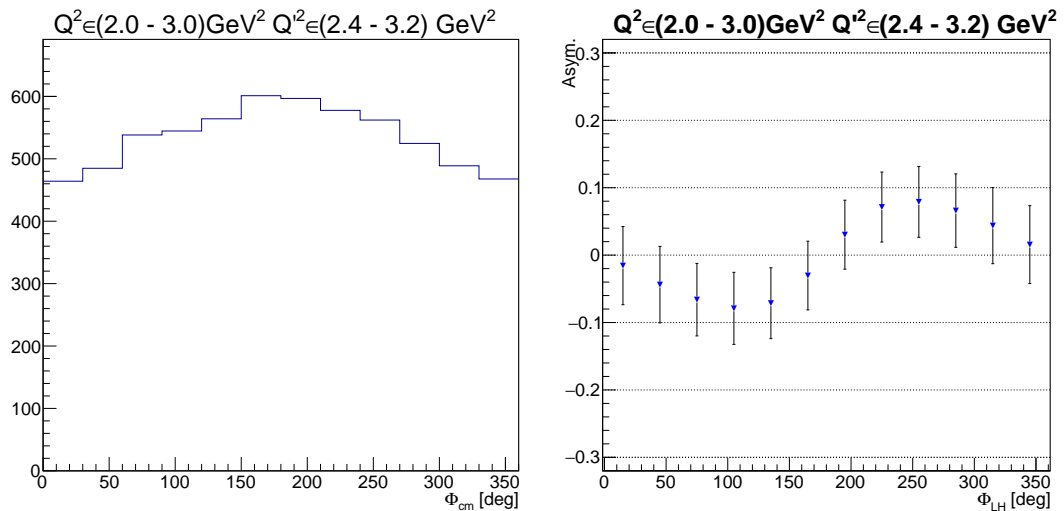


FIG. 35: Count rates (left) and statistic error-bars (right) for the $Q'^2(2.4 – 3.2) \text{ GeV}^2$ bin.

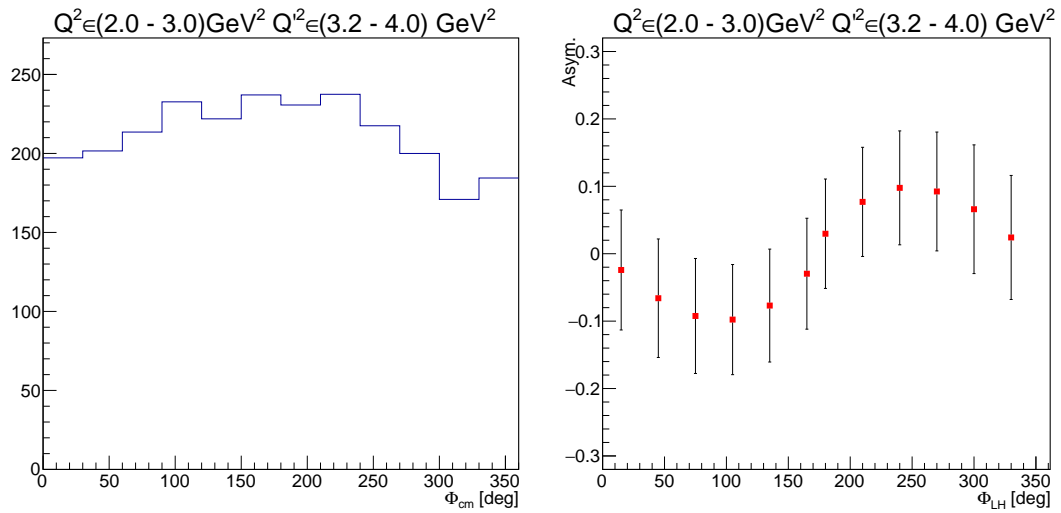


FIG. 36: Count rates (left) and statistic error-bars (right) for the $Q'^2(3.2 - 4) \text{ GeV}^2$ bin.

B. J/ψ Electroproduction

To estimate cross section we used Vector Dominance Model (VDM) [68] to relate electroproduction cross section to the photoproduction cross section. For the photoproduction cross section the 2-gluon exchange model from [43] was used. Cross section for electroproduction can be presented as a sum of the cross sections for transversely (σ_T), and longitudinally (σ_L) polarized photons:

$$\frac{d\sigma_{eN \rightarrow eM^0 N}}{dQ^2 dW dt} = \Gamma_W \cdot \left(\frac{d\sigma_T}{dt} + \epsilon \frac{d\sigma_L}{dt} \right). \quad (11)$$

Here Γ_W is the flux of virtual photons and is defined as:

$$\Gamma_W = \frac{\alpha}{4\pi} \cdot \frac{W^2 - m^2}{m^2 E^2} \cdot \frac{W}{Q^2} \cdot \frac{1}{1 - \epsilon}. \quad (12)$$

and the ϵ is the virtual photon polarization:

$$\epsilon = \left(1 + 2 \frac{Q^2 + q^{02}}{4EE' - Q^2} \right)^{-1}. \quad (13)$$

Using vector meson dominance (VDM) one can relate σ_T and σ_L to the photoproduction cross section [68]:

$$\sigma_T = \left(\frac{m_{J/\Psi}^2}{m_{J/\psi}^2 + Q^2} \right)^2 \cdot \sigma_{\gamma N \rightarrow M^0 N}, \quad (14)$$

and

$$\sigma_L = \left(\frac{m_{J/\Psi}^2}{m_{J/\psi}^2 + Q^2} \right)^2 \cdot \frac{Q^2}{m_{J/\psi}^2} \cdot (1-x)^2 \cdot \xi(Q^2, \nu) \cdot \sigma_{\gamma N \rightarrow M^0 p}, \quad (15)$$

where $m_{J/\psi}$ is the J/ψ meson mass. $\xi(Q^2, \nu)$ scales the model to the data, and is taken to be 0.5 for our calculations. The $x = Q^2/(2qp)$ where p is the four-momentum of the target nucleon. The $\sigma_{\gamma N \rightarrow M^0 N'}$ is the photoproduction cross section.

The description of the photoproduction cross section for the 2-gluon exchange formalism, see Figure 37, is taken from [43]:

$$\frac{d\sigma}{dt} = N_{2g} \nu \frac{(1-x)^2}{R^2 M^2} F_{2g}^2(t) (s - m_p^2)^2 \quad (16)$$

where $F_{2g}(t)$ is the proton form factor that takes into account the fact that the three target quarks recombine into the final proton after the emission of two gluons. The N_{2g} is scaling factor to saturate measured cross sections as shown in Figure 38. The M is the mass of the $c\bar{c}$, R is the proton radius, taken as 1 fm, s is the center-of-mass energy square and the x is the fraction of the proton momentum carried by the valence quark.

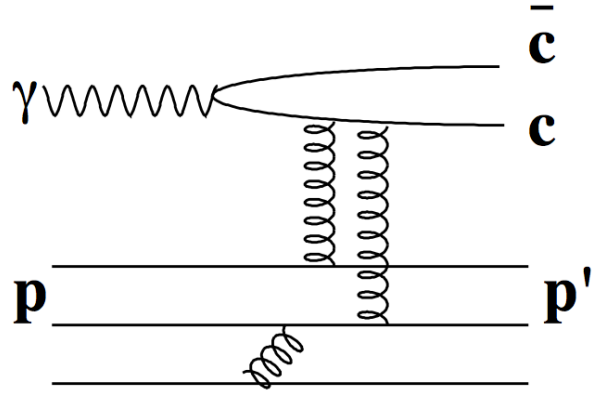


FIG. 37: Diagram for $c\bar{c}$ photoproduction on the nucleon via 2-gluon exchange.

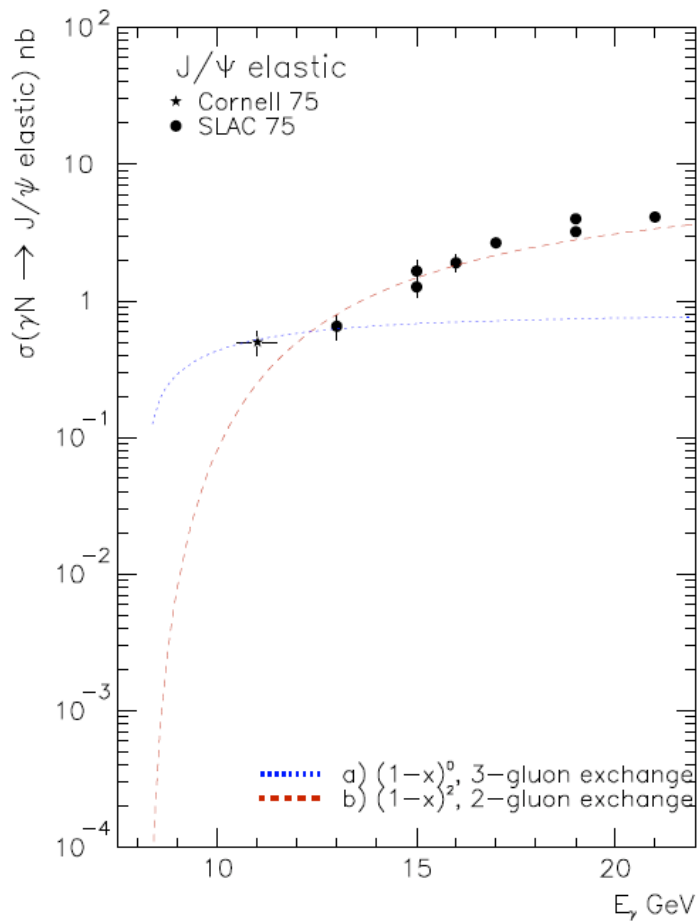


FIG. 38: J/ψ photoproduction cross section as a function of incoming photon energy from [43]. Dashed and dotted curves are descriptions cross section via 2-gluon and 3-gluon exchange models, respectively.

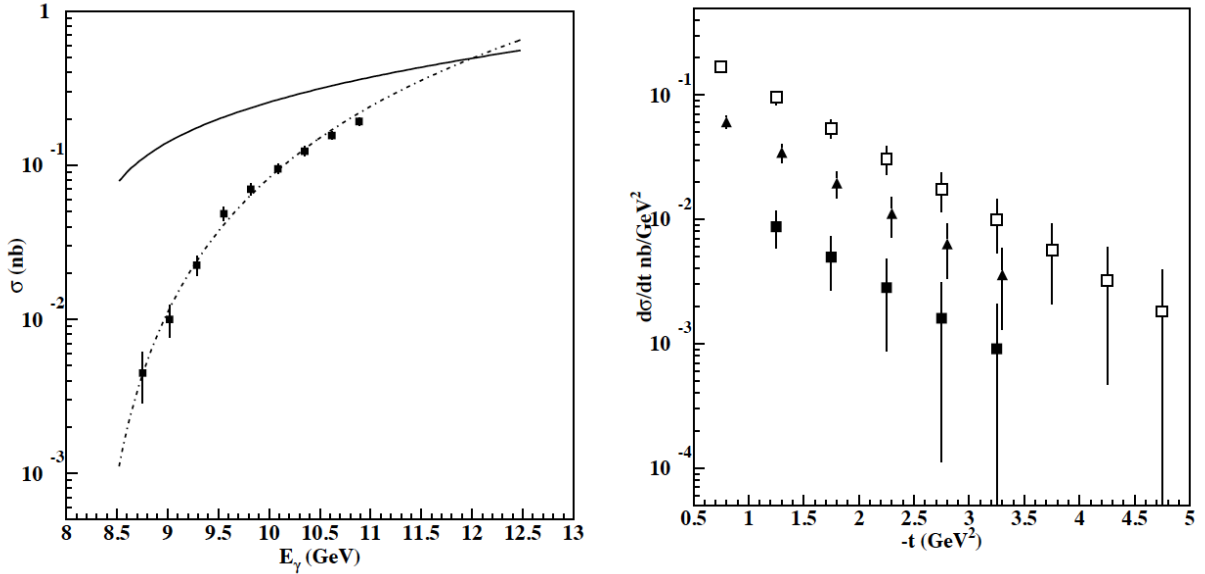


FIG. 39: The cross section of exclusive J/ψ photoproduction for 100 days of running from [47].

On the left: total cross section as a function of the incoming photon energy. The curves are calculated according to cross section formulas in Ref. [43]. On the right: Differential cross section as a function of the squared four momentum transferred $-t$ for three bins of s . The dashed line and the filled squares are for $s = 17.55$ to 18.05 GeV^2 , the dotted line and the inverted filled triangles are for $s = 19.05$ to 19.55 GeV^2 , and the dashed-dotted line and the open squares are for $s = 21.05$ to 21.55 GeV^2 .

This cross section model has been used to calculate expected rates for the experiment E-12-12-001 [47]. If there is an enhancement of the cross section in the region $E_\gamma < 11$ GeV , for example due to 3-gluon exchange production as proposed in [43], then clearly the estimated rates presented below are quite conservative. The expected results for E_γ - and t -dependences of exclusive J/ψ photoproduction cross section from E12-12-001 proposal are shown in Figure 39 as a reference. The same code was used to calculate cross sections for the electroproduction cross section in the kinematics of the present proposal. In Figure 40, the t -dependence of the differential cross section for three (Q^2 , W) points are shown. Due to strong Q^2 dependence of the available W range (see Figure 10) the t -ranges are different for each Q^2 .

For these studies a general purpose event generator [69] that allows to simulate multi-particle final states in photo- and electroproduction reactions with user defined kinematic dependancies, e.g. Q^2 and t , and with correct decay branching ratios for most of particles listed in PDG (Lund/Jetset

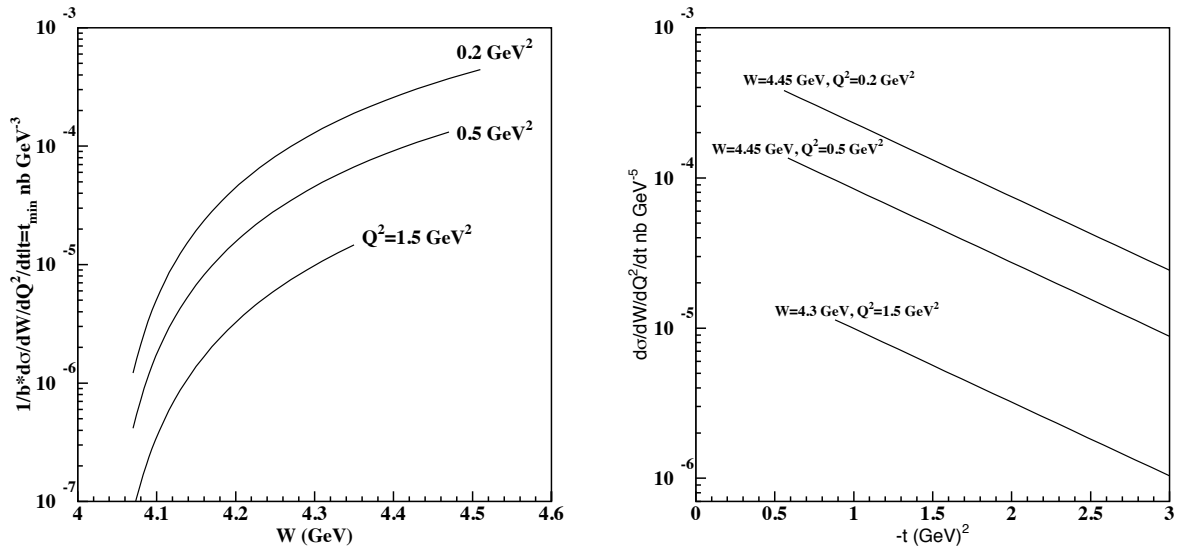


FIG. 40: The differential cross section of J/ψ electroproduction as a function of squared transferred momentum for three (Q^2 , W) points.

[70]) was used. The detector response was simulated using the modified CLAS12 Fast MC algorithm. This algorithm has correct geometrical acceptance of CLAS12, and the parametrization of the momentum and angular resolutions. Since muons will be detected in CLAS12 FD after passing through 20 cm long PbWO₄ modules and a 30 cm thick tungsten absorber, momentum of muons before CLAS12 acceptance and smearing functions was recalculated to take into account energy loss using realistic profile of the muon energy loss. After smearing in CLAS12, an average energy loss value was added to the momentum to retrieve value of particle momentum at the vertex. Also, additional smearing term was added to the angular resolution to account for multiple scattering of muons in the material of the calorimeter and absorber. For electron detection a new detector was introduced in fast MC. The geometrical acceptance of the detector was confined within polar angle $\theta = 7^\circ$ to 30° with $\phi = 2\pi$ azimuthal coverage. Detection energy threshold was set to $p > 0.5$ GeV/c. The energy resolution of $\sigma_E/E = 3.7\%/\sqrt{(E)}$ and the angular resolution of $\sigma_{\theta(\phi)} = 2$ mrad were taken from analysis of the performance of a similar calorimeter used for the Hall-B HPS experiment [71].

The reaction $ep \rightarrow e' J/\psi p' \rightarrow e' \mu^+ \mu^- p'$ was simulated with conditions described in Section III. The momentum vs. scattering angle distributions for all final state particles are shown in Figure 41. Due to a large momentum transfer near the J/ψ production threshold, the recoil proton scatters

in forward direction, $\theta_p < 30^\circ$, and will not be detected. Muons are produced mostly in forward angles ($\theta_\mu < 40^\circ$), bottom left panel of Figure 41, and remain in the same momentum-angular space when electrons are detected in the calorimeter, bottom right panel of the figure. The CLAS12 FD that can detect changed tracks in angular range $5^\circ < \theta < 35^\circ$ well suited for detecting muons from presented reaction. In Fig.42 momentum vs scattering angle of μ^+ and μ^- detected in CLAS12 FD are shown. Since muons in average have large momentum there is not much difference in detection efficiencies for negatively and positively charged tracks at forward angles, which is present for low momentum tracks due to the toroidal magnetic field and the CLAS12 detector coverage.

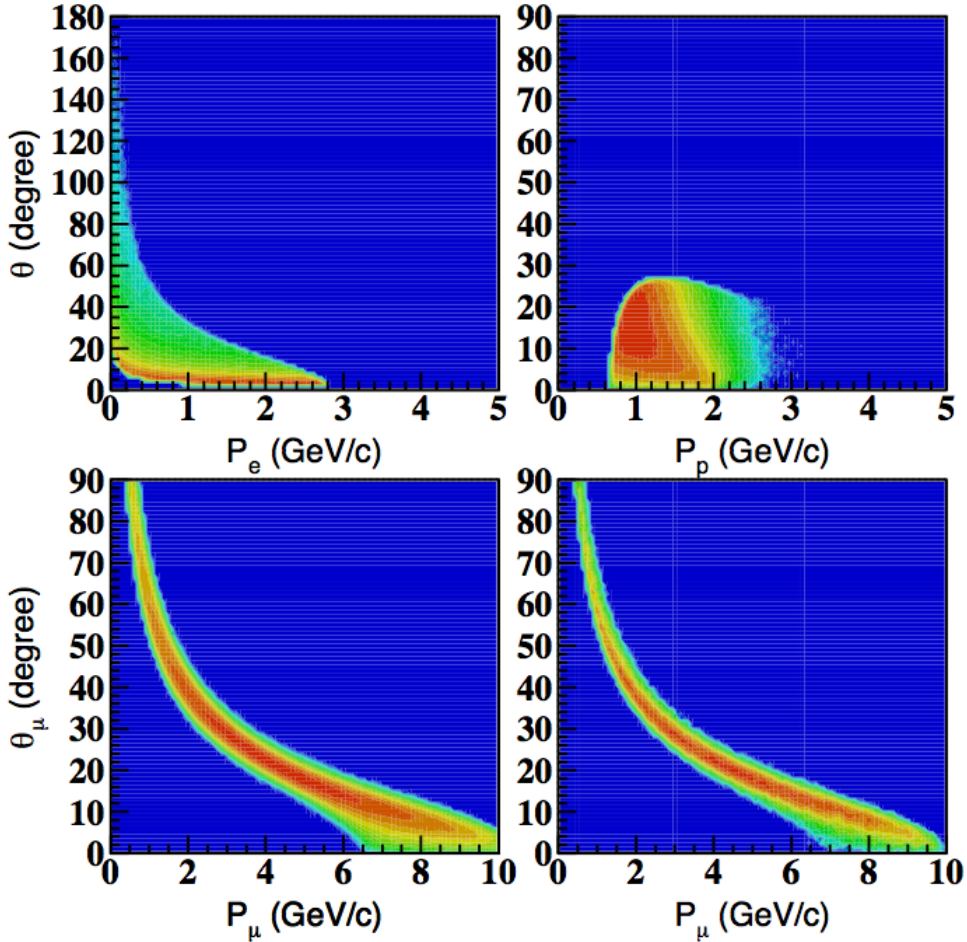


FIG. 41: Kinematics of the scattered electron, recoil proton, and the decay muons for the reaction $ep \rightarrow e'p'J/\Psi$. In the bottom-right panel angular-momentum distribution of muons is shown for events where electron momentum is $p > 0.5$ GeV and is in the scattering angular range

$$5^\circ < \theta < 35^\circ.$$

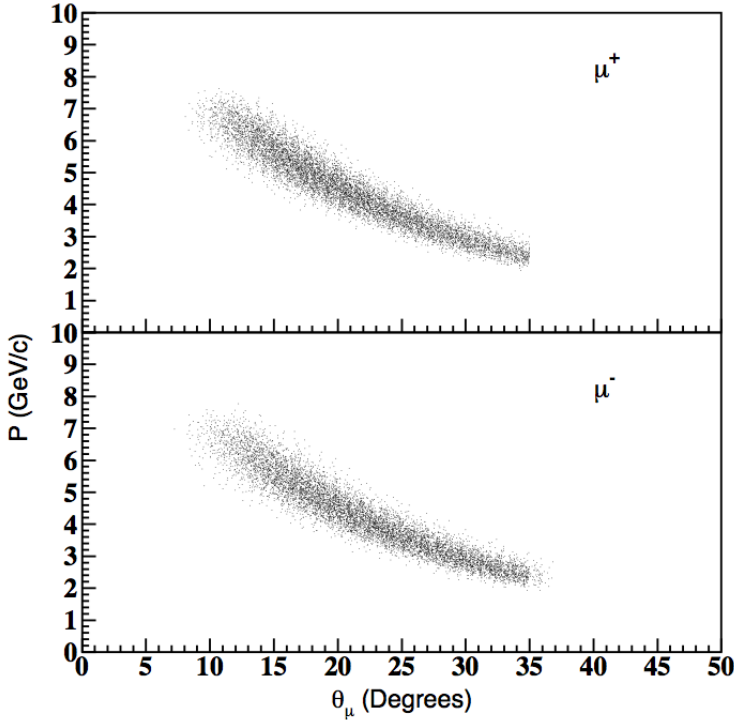


FIG. 42: Angular-momentum distributions of μ^+ (top) and μ^- bottom detected in the CLAS12 FD.

Since the recoil proton will not be detected, when exclusivity is required the missing momentum analysis of the $e\mu^+\mu^-$ final state will be performed to select events in the reaction $ep \rightarrow e'p'J/\psi$, after identifying the J/ψ in the invariant mass of the muon pairs. For this, the mass (invariant and missing) resolutions will play an important role in identification of the reaction. In Fig.43, expected resolutions for invariant and missing masses are shown when the field strength of the CLAS12 toroidal magnet was set to 75% of its maximum. These distributions have been calculated using reconstructed, smeared, 3-momenta of the electron, μ^+ and μ^- . Both distributions are fitted with Gaussian function. The standard deviation for $\mu^+\mu^-$ invariant mass is ~ 60 MeV, the missing mass resolution of $e\mu^+\mu^-$ is ~ 80 MeV, sufficient for identification of the J/ψ and the missing recoil proton.

As was described in Section III, the goal of the J/ψ electroproduction studies is to measure the W and t -dependence of the cross section at different values of Q^2 , as well as to study decay angular distributions of muons in order to extract σ_L/σ_T ratio. For this, detector efficiencies were studied in three regions of Q^2 , $0.1 < Q^2 < 0.3$ GeV 2 , $0.3 < Q^2 < 1$ GeV 2 , and $1 < Q^2 < 2.5$ GeV 2 .

Acceptances, averaged over Q^2 , as a function W and t for three Q^2 bins are shown in Fig.44.

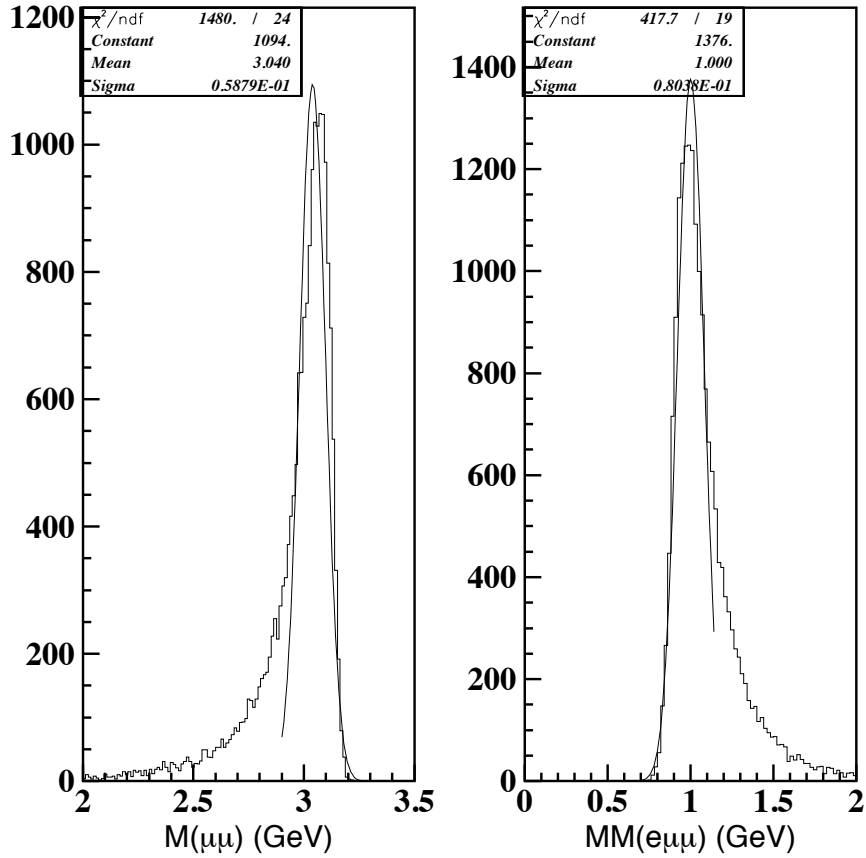


FIG. 43: Expected mass resolutions for of 75% of CLAS12 torus magnet maximum field setting.

Left the invariant mass of muon pairs, right the missing mass squared for the reaction

$$ep \rightarrow e'\mu^+\mu^-(p).$$

The acceptance for detection of $(e\mu^+\mu^-)$ when the toroidal magnet field setting is 75% of its max is about $\sim 8\%$ (somewhat lower for the lowest Q^2 bin). The same simulations showed that the coverage for decayed muon angular range in the J/ψ rest frame for different Q^2 bins is the same. Overall coverage for $\cos\theta^*$ is from -0.5 to 0.5 , while in ϕ^* is $\sim 2\pi$ with holes corresponding to the CLAS12 blind spots due to the toroidal magnet coils, see left panel of Figure 45. The acceptance as a function of $\cos\theta^*$ for three bins of Q^2 is shown on the right panel of the figure. Again the lowest Q^2 bin has the smallest acceptance. These acceptances for each of W , t and $\cos\theta^*$ distributions were obtained after integration over two other parameters. For rate estimate 2D acceptances with finer bins in t and W were used.

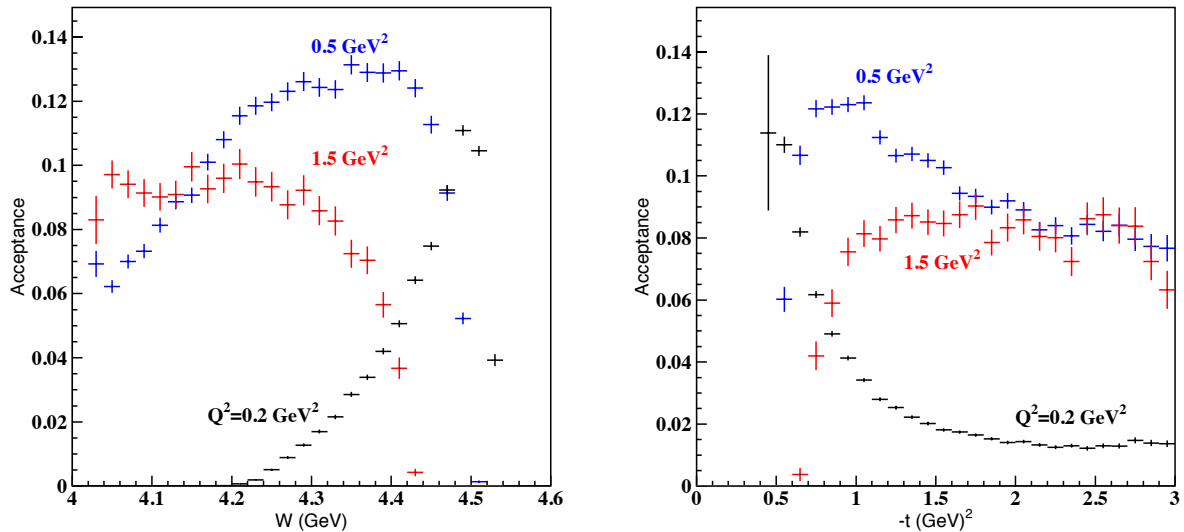


FIG. 44: Acceptances as a function of W and t for three Q^2 bins.

In Figure 46.a the invariant mass of muon pairs integrated over W , t and Q^2 is shown for 100 days of running at luminosity of 10^{37} cm $^{-2}$ sec $^{-1}$. The invariant mass distributions for three different Q^2 bins centered at $Q^2 = 0.2$ GeV 2 , 0.5 GeV 2 , and 1.5 GeV 2 are shown in Figure 46.b, c, and d. The J/ψ peak is clearly visible of Bethe-Heitler background that has been simulated using the GRAPE-dilepton event generator [65]. In the analysis fit with a background function and Gaussian will be used to extract number of J/ψ 's in each kinematic bin.

The t -dependences of the differential cross sections, integrated over Q^2 and W , for three Q^2 bins, 0.2 GeV 2 , 0.5 GeV 2 , and 1.5 GeV/c 2 are shown in the top graph of Figure 47. The expected uncertainties on the points have been estimated assuming 100 days of running at luminosity of 10^{37} cm $^{-2}$ sec $^{-1}$. The values of cross sections, expected statistical errors, and the rates for t -dependence measurements are presented in Table I. The total center-of-mass energy dependence of the differential cross sections after integration over transferred momentum squared are shown in the bottom of Figure 47 and in Table II. Again expected statistical errors and rates correspond to 100 days of running at luminosity of 10^{37} cm $^{-2}$ sec $^{-1}$. A total of ~ 9000 J/ψ -mesons are expected to be detected.

One should note, since the experiment will run with a two MIP particle trigger in CLAS12 FD, J/ψ -mesons from quasi-real photoproduction ($Q^2 \sim 0$) will be detected as well. With the proposed luminosity we will collect, for example, 4 J/ψ per hour in 0.1 GeV energy bin at incoming photon

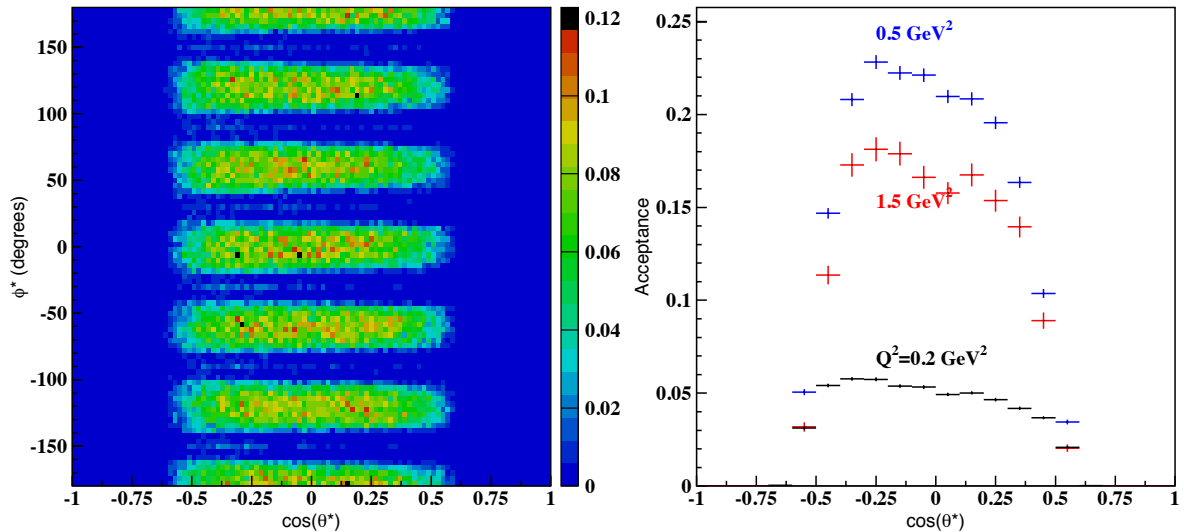


FIG. 45: On the left is acceptances (color scheme) as a function of ϕ^* and $\cos\theta^*$ of μ^+ in the J/ψ rest frame. On the right acceptances as a function of $\cos\theta^*$ for three Q^2 bins.

energy of 10 GeV. With such high rate of J/ψ production, detailed studies of $J/\psi N$ interaction can be done in experiments with nuclear targets.

C. Rates for pentaquarks

Similar to J/ψ case, VDM was used to derive electroproduction cross section from predicted photoproduction cross section. Fig. 48 illustrates the $P_c(4450)$ pentaquark formation cross section as a function of the photon beam energy for two cases [51]. The left panel corresponds to the presence of only the lower allowed partial wave. The right panel shows the same cross section for the upper bound where only the higher orbital wave is present. The vertical lines represent the resonant energy $E_0 = 10.1$ GeV and the boundaries of the region $M_c \pm \Gamma/2$ in the laboratory system that contains 50% of the total production cross section. The calculations were done with $Br(P_c \rightarrow J/\psi p) = 1\%$. The cross section is proportional to $Br^2(P_c \rightarrow J/\psi)$. If the J/ψ meson will be detected in the $\mu^+\mu^-$ decay mode we need to take into account the branching ratio $Br(J/\psi \rightarrow \mu^+\mu^-) = 6\%$.

In order to search pentaquark states, especially narrow $P_c(4450)$, reasonably good W resolution is required. The resolution in W is presented in Fig. 49. We have to compare 10 MeV detector resolution with the width of pentaquark that is around 40 MeV for $P_c(4450)$ and 200 MeV for

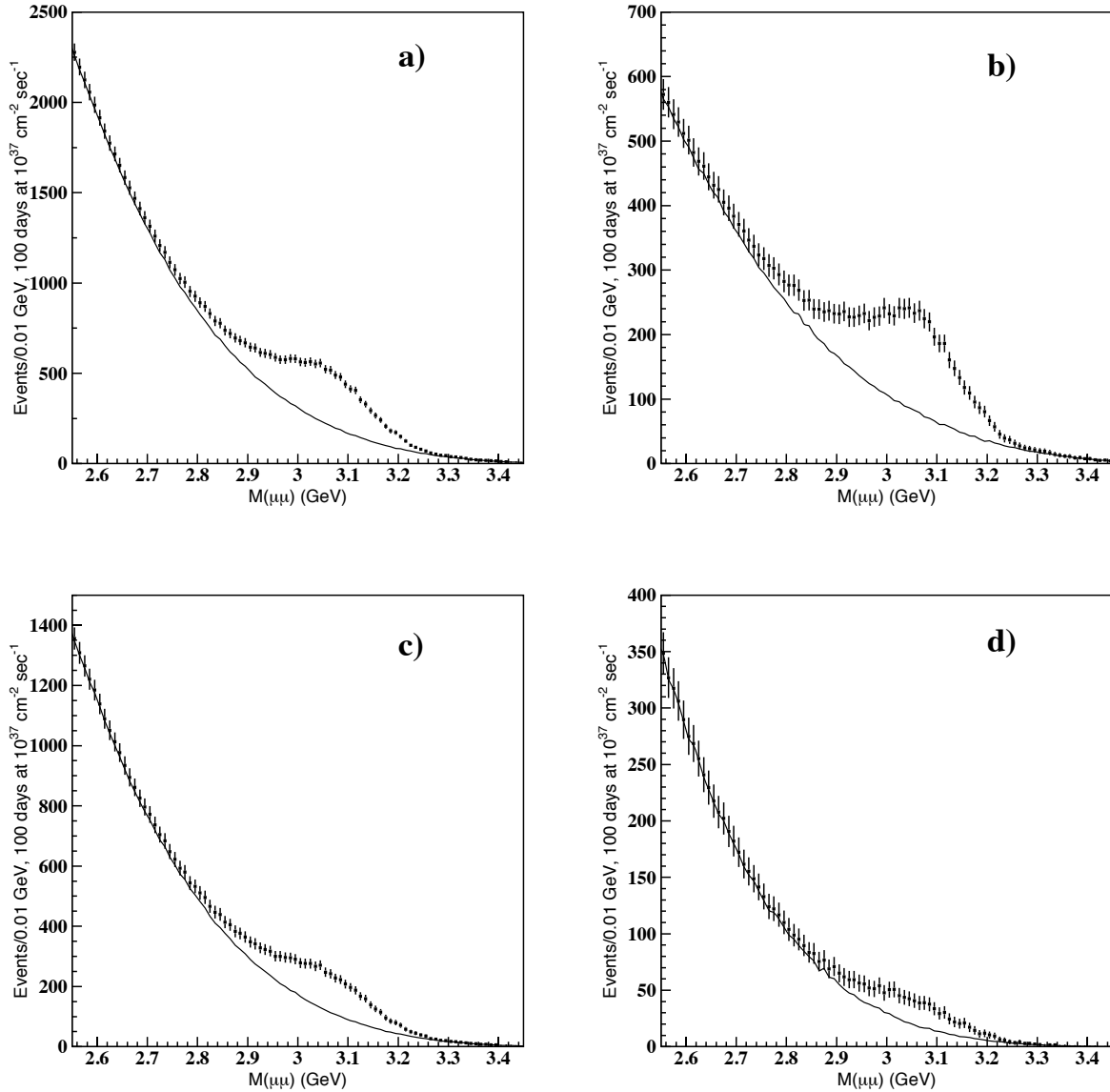


FIG. 46: The invariant mass distribution of muon pairs integrated over W , and t for full Q^2 range, (a), and for three different Q^2 bins centered at $Q^2 = 0.2 \text{ GeV}^2$, 0.5 GeV^2 , and 1.5 GeV^2 , (b), (c), and (d), respectively. The background under the peak is realistic simulation of Bethe-Heitler. Error bars are statistical and correspond to 100 days of running at luminosity of $10^{37} \text{ cm}^{-2} \text{ sec}^{-1}$

$P_c(4380)$. We see that even for narrow pentaquark the W resolution is satisfactory.

The pentaquark yield for one day at the proposed luminosity is presented in the Table III for two states and two values of the predicted cross sections [51], assuming $Br(P_c \rightarrow J/\psi p) = 1\%$. The elastic J/ψ photoproduction has cross section $\sigma \approx 0.1 \text{ nb}$ at $W = 4.45 \text{ GeV}$. Integrated over

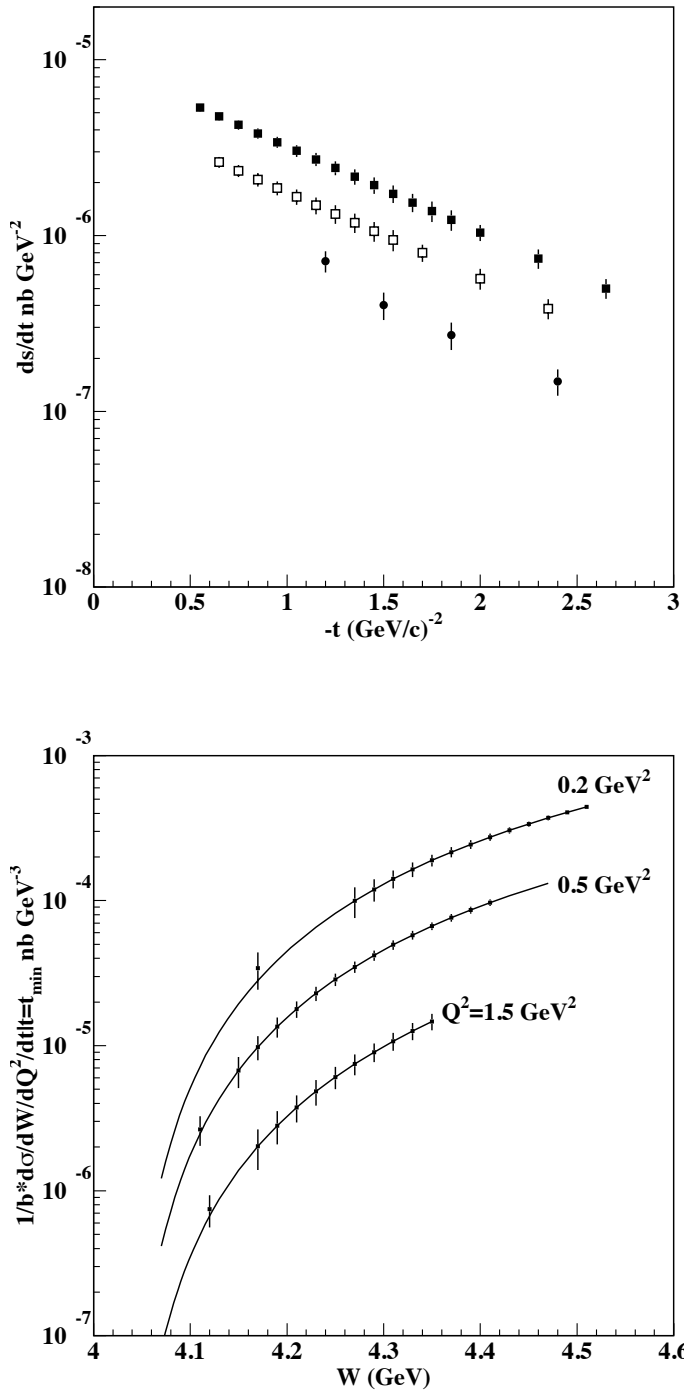


FIG. 47: Top graph: differential cross section and expected statistical errors as a function of squared transferred momentum for three Q^2 bins with mean values of $Q^2 = 0.2 \text{ GeV}^2$, 0.5 GeV^2 , and 1.5 GeV^2 , integrated over W . Bottom: differential cross section at $t = t_{\min}$ as a function of W for three Q^2 bins.

TABLE I: Differential cross section, $\frac{d\sigma}{dt}$, integrated over Q^2 and W , as a function of transferred momentum squared. The error, $\delta\sigma$, is calculated based on the expected statistics ($N_{J/\psi}$) for 100 days of running at luminosity of $10^{37} \text{ cm}^{-2} \text{ sec}^{-1}$.

$\bar{Q}^2 = 0.2 \text{ GeV}^2$				$\bar{Q}^2 = 0.5 \text{ GeV}^2$				$\bar{Q}^2 = 1.5 \text{ GeV}^2$			
t (GeV 2)	σ	$\delta\sigma$	$N_{J/\psi}$	t	σ	$\delta\sigma$	$N_{J/\psi}$	t	σ	$\delta\sigma$	$N_{J/\psi}$
-0.55	0.53E-05	0.29E-06	346.4	-0.65	0.26E-05	0.19E-06	184.6	-0.95	0.56E-06	0.10E-06	31.7
-0.65	0.48E-05	0.28E-06	296.3	-0.75	0.23E-05	0.18E-06	162.9	-1.05	0.62E-06	0.11E-06	32.6
-0.75	0.43E-05	0.26E-06	262.5	-0.85	0.21E-05	0.18E-06	132.7	-1.20	0.71E-06	0.98E-07	52.8
-0.85	0.38E-05	0.25E-06	223.1	-0.95	0.19E-05	0.17E-06	118.0	-1.50	0.40E-06	0.72E-07	31.5
-0.95	0.34E-05	0.25E-06	190.9	-1.05	0.17E-05	0.17E-06	98.1	-1.85	0.27E-06	0.49E-07	31.2
-1.05	0.30E-05	0.23E-06	169.5	-1.15	0.15E-05	0.16E-06	82.0	-2.40	0.15E-06	0.25E-07	34.0
-1.15	0.27E-05	0.23E-06	135.7	-1.25	0.13E-05	0.16E-06	69.8				
-1.25	0.24E-05	0.22E-06	123.3	-1.35	0.12E-05	0.15E-06	62.0				
-1.35	0.22E-05	0.21E-06	101.5	-1.45	0.11E-05	0.13E-06	62.1				
-1.45	0.19E-05	0.21E-06	88.1	-1.55	0.95E-06	0.13E-06	52.1				
-1.55	0.17E-05	0.20E-06	77.0	-1.70	0.80E-06	0.89E-07	79.7				
-1.65	0.15E-05	0.18E-06	71.3	-2.00	0.57E-06	0.76E-07	55.6				
-1.75	0.14E-05	0.18E-06	57.6	-2.35	0.38E-06	0.50E-07	58.8				
-1.85	0.12E-05	0.16E-06	56.7								
-2.00	0.10E-05	0.11E-06	88.4								
-2.30	0.74E-06	0.93E-07	63.0								
-2.65	0.50E-06	0.64E-07	60.3								

40 MeV bin yield is 12 events/day. It is 8% from the expected pentaquark $P_c(4450)$ production with $\Gamma = 40$ MeV.

TABLE II: The W-averaged J/ψ electroproduction differential cross section as a function of transferred momentum squared. The error, $\delta\sigma$, is calculated based on the expected rates ($N_{J/\psi}$) for 100 days of running at luminosity of $10^{37} \text{ cm}^{-2} \text{ sec}^{-1}$.

$\bar{Q}^2 = 0.2 \text{ GeV}^2$				$\bar{Q}^2 = 0.5 \text{ GeV}^2$				$\bar{Q}^2 = 1.5 \text{ GeV}^2$			
W GeV	σ nb GeV^{-3}	$\delta\sigma$ nb GeV^{-3}	$N_{J/\psi}$	W GeV	σ nb GeV^{-3}	$\delta\sigma$ nb GeV^{-3}	$N_{J/\psi}$	W GeV	σ nb GeV^{-3}	$\delta\sigma$ nb GeV^{-3}	$N_{J/\psi}$
4.17	0.34E-04	0.98E-05	12.1	4.11	0.26E-05	0.60E-06	19.2	4.12	0.75E-06	0.19E-06	16.0
4.27	0.10E-03	0.24E-04	17.7	4.15	0.67E-05	0.16E-05	17.1	4.17	0.20E-05	0.63E-06	10.3
4.29	0.12E-03	0.21E-04	32.4	4.17	0.98E-05	0.19E-05	27.6	4.19	0.28E-05	0.72E-06	15.0
4.31	0.14E-03	0.20E-04	49.7	4.19	0.13E-04	0.21E-05	40.9	4.21	0.37E-05	0.79E-06	22.4
4.33	0.16E-03	0.19E-04	74.7	4.21	0.18E-04	0.23E-05	60.5	4.23	0.48E-05	0.96E-06	25.2
4.35	0.19E-03	0.18E-04	115.0	4.23	0.23E-04	0.26E-05	77.7	4.25	0.61E-05	0.10E-05	33.5
4.37	0.22E-03	0.17E-04	155.0	4.25	0.29E-04	0.29E-05	98.1	4.27	0.75E-05	0.12E-05	36.4
4.39	0.24E-03	0.16E-04	220.4	4.27	0.35E-04	0.31E-05	123.3	4.29	0.90E-05	0.13E-05	47.7
4.41	0.27E-03	0.16E-04	287.8	4.29	0.42E-04	0.34E-05	154.3	4.31	0.11E-04	0.15E-05	50.7
4.43	0.30E-03	0.15E-04	418.4	4.31	0.50E-04	0.37E-05	180.2	4.33	0.13E-04	0.17E-05	54.8
4.45	0.34E-03	0.15E-04	535.7	4.33	0.58E-04	0.41E-05	203.7	4.35	0.15E-04	0.19E-05	59.8
4.47	0.37E-03	0.14E-04	729.1	4.35	0.67E-04	0.42E-05	247.8				
4.49	0.41E-03	0.13E-04	940.9	4.37	0.76E-04	0.45E-05	286.0				
4.51	0.44E-03	0.14E-04	967.3	4.39	0.86E-04	0.48E-05	317.5				

TABLE III: Estimated number of detected by CLAS events.

	$\sigma(W = M_c)$	Number of events per day
	Minimum - Maximum	Minimum - Maximum
$P_c(4380)$	0.15 - 4.7 nb	150 - 4700
$P_c(4450)$	1.2 - 36 nb	230 - 7000

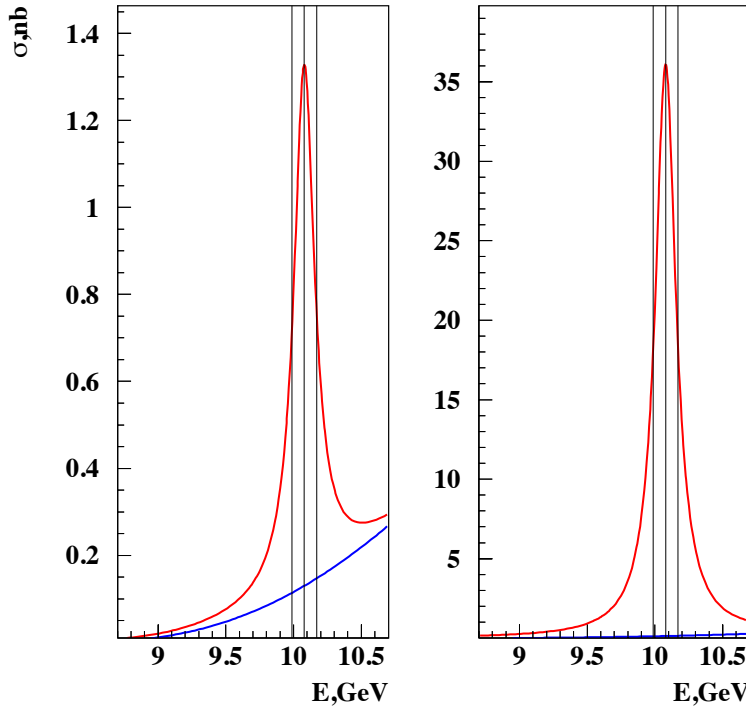


FIG. 48: The $P_c(4450)$ resonance formation cross section in the reaction $\gamma p \rightarrow P_c \rightarrow J/\psi p$ as a function of the photon energy in the region of the CLAS acceptance. Two panels represent the theoretical uncertainty due to the unknown composition of the partial waves (see text for details). The vertical lines represent the resonant energy $E_0 = 10.1$ GeV and the boundaries of the region $M_c \pm \Gamma/2$ in the laboratory system. The two curves show the elastic background [43] and Breit-Wigner distribution. The calculations were done assuming $Br(P_c \rightarrow J/\psi p) = 1\%$.

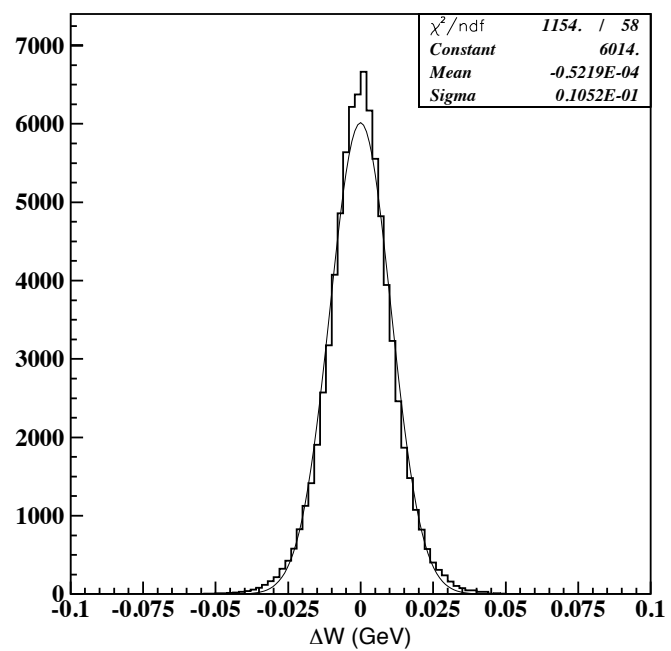


FIG. 49: Resolution in W.

VI. SUMMARY AND BEAM TIME REQUEST

We propose to study DDVCS and J/ψ electroproduction on the proton using the 11 GeV electron beam and a modified CLAS12 detector in experimental Hall-B at Jefferson lab. The beam spin asymmetry in DDVCS will be measured at several values of space-like and time-like virtualities of incoming and outgoing virtual photons, respectively. The DDVCS allows to decorrelate the two variables, x and ξ , and access x independently of ξ , clearly yielding precious new information on GPDs otherwise unaccessible.

In the same experiment, J/ψ production near threshold will be studied to provide valuable information on the gluonic structure of the proton. Measurements will provide J/ψ electroproduction cross sections as a function of the total center of mass energy, W , and the squared transferred momentum, t , for several Q^2 values. Analysis of the decay angular distributions of muons will allow to extract σ_L/σ_T for the first time at close to the production threshold region.

Proposed modifications to the CLAS12 detector for these measurements are aimed to serve two purposes (a) allow the CLAS12 Forward Detector to run at orders of magnitude higher luminosities than the design luminosity, and (b) convert the CLAS12 FD into a muon detector. The scattered electrons in this new setup will be detected and identified in a new, compact, PbWO₄ electromagnetic calorimeter. Preliminary cost estimate for modification is $\sim \$4$ M.

We request 100 days of beam time and intend to run modified CLAS12 at luminosity of 10^{37} cm $^{-2}$ sec $^{-1}$. The GEANT4 simulations using proposed modifications, PbWO₄ calorimeter, GEM tracker, and a 30 cm thick shield/absorber, show that the occupancies in the detector, and the trigger rates and background in final state identification are manageable.

-
- [1] JLAB proposals for studying GPDs using the Deeply Virtual Compton Scattering, E12-06-119, E12-11-003, E12-06-114, E12-13-010.
- [2] JLAB proposals for studying GPDs using the Deeply Virtual Meson Production, E12-12-007.
- [3] JLAB Letter of Intents, and proposal for studying GPDs using Timelike Compton Scattering: LOI12-15-007, E12-12-001.
- [4] A. Aktas et al. H1 Coll. *Eur. Phys. J.* **C46**, 585-603 (2006).
- [5] S. Chekanov et al. ZEUS Coll. *Nucl. Phys.* **B695**, 3-37 (2004).
- [6] M.E. Binkley et al. *Phys. Rev. Lett.* **44**, 73 (1982).
- [7] J. Breitweg et al. ZEUS Coll. *Eur. Phys. J. C* **6**, 603 (1999).
- [8] C. Adloff et al. H1 Coll. *Eur. Phys. J. C* **13**, 371 (2000).
- [9] C. Adloff et al. H1 Coll. *Phys. Lett. B* **539**, 25 (2002).
- [10] CLAS12 conceptual design report, <https://www.jlab.org/Hall-B/clas12\tdr.pdf>.
- [11] K. Goeke, M. V. Polyakov, and M. Vanderhaeghen. *Prog. Part. Nucl. Phys.* **47** 401 (2001).
- [12] M. Diehl. *Phys. Rept.* **388** 41 (2003).
- [13] A.V. Belitsky and A.V. Radyushkin. *Phys. Rept.* **418** 1 (2005).
- [14] M. Guidal, H. Moutarde, and M. Vanderhaeghen. *Rept. Prog. Phys.* **76** 066202 (2013).
- [15] E. R. Berger, M. Diehl, and B. Pire. *Eur. Phys. J. C* **23** 675 (2002).
- [16] A. T. Goritschnig, B. Pire, and J. Wagner. Timelike Compton scattering with a linearly polarized photon beam. *arXiv:1404.0713 [hep-ph]*.
- [17] M. Boér, M. Guidal, and M. Vanderhaeghen. Single and double polarization observables in timelike Compton scattering off proton. *arXiv:1501.00270 [hep-ph]*.
- [18] X D Ji. Deeply virtual Compton scattering. *Phys. Rev. D* **55** 7114, 1997.
- [19] M. Vanderhaeghen, P.A.M. Guichon, and M. Guidal. *Phys. Rev. D* **60**, 094017 (1999).
- [20] C. Muñoz Camacho et al. *Phys. Rev. Lett.* **97**, 262002 (2006).
- [21] M. Defurne et al. *Phys. Rev. C* **92** (2015) 055202.
- [22] H. S. Jo et al. Cross sections for the exclusive photon electroproduction on the proton and Generalized Parton Distributions. *Phys. Rev. Lett* **115** (2015) 212003, *arXiv:1504.02009 [hep-ex]*.
- [23] F.-X. Girod et al. *Phys. Rev. Lett.* **100**, 162002 (2008).
- [24] S. Chen et al. *Phys. Rev. Lett.* **97**, 072002 (2006).
- [25] E. Seder et al. *Phys. Rev. Lett.* **114** 3 (2015).
- [26] S. Pisano et al. [CLAS Collaboration]. Single and double spin asymmetries for deeply virtual Compton scattering measured with CLAS and a longitudinally polarized proton target. *Phys. Rev. D* **91** (2015) 5, 052014 [*arXiv:1501.07052 [hep-ex]*].
- [27] K. Kumericki and D. Müller. *Nucl. Phys. B* **841**, 1 (2010).
- [28] H. Moutarde. *Phys. Rev. D* **79**, 094021 (2009).

- [29] M. Guidal. *Eur. Phys. J. A* **37**, 319 (2008) [*Erratum-ibid.A40:119,2009*].
- [30] M. Guidal and H. Moutarde. *Eur. Phys. J. A* **42**, 71 (2009).
- [31] M. Guidal. *Phys. Lett. B* **689** (2010) 156.
- [32] M. Guidal. *M. Guidal, Phys. Lett. B* **693** (2010) 17.
- [33] M. Burkardt. Impact parameter dependent parton distributions and off-forward parton distributions for $\zeta \rightarrow 0$. *Phys. Rev. D* **62** 071503 (2000).
- [34] M. Guidal and M. Vanderhaeghen. Double deeply virtual Compton scattering off the nucleon. *Phys. Rev. Lett.* **90** (2003) 012001.
- [35] A. V. Belitsky and D. Mueller. *Phys. Rev. Lett.* **90**, 022001 (2003).
- [36] A. V. Belitsky and D. Mueller. *Phys. Rev.D* **68**, 116005 (2003).
- [37] D. Mueller, B. Pire, L. Szymanowski, and J. Wagner. On timelike and spacelike hard exclusive reactions. *Phys. Rev. D* **86** (2012) 031502.
- [38] A. Accardi et al. *arxiv 1212.1701* (2012).
- [39] N. Brambilla et al. *Eur. Phys. J.* **C71**, 1534 (2011).
- [40] L. Frankfurt, M. Strikman, and Ch. Weiss. *Ann. Rev. Nucl. Part. Sci.* **55**, 403-465 (2005).
- [41] C. Weiss and M. Strikman. *Workshop on Non-Perturbative Color Forces in QCD, Temple University, Philadelphia, PA* (2012).
- [42] L. Frankfurt and M. Strikman. *Phys. Rev.*, **D66**, 031502 (2002).
- [43] S.J. Brodsky, E. Chudakov, P. Hoyer, and J.M. Laget. *Phys. Lett. B* **498**, pp. 23-29 (2001).
- [44] M. Butenschoen and B. Kniehl. *Phys. Rev. Lett.* **104**, 072001 (2010).
- [45] M. Butenschoen and B. Kniehl. *Phys. Rev.* **D84**, 051501 (2011).
- [46] M. Butenschoen and B.A. Kniehl. *Workshop on Non-Perturbative Color Forces in QCD, Temple University, Philadelphia, PA* (2012).
- [47] P. Nadel-Turonski et al. *Timelike Compton Scattering and J/psi photoproduction on the proton in e+e- pair production with CLAS12 at 11 GeV*, E12-12-001 (2012).
- [48] K. Schilling and G. Wolf. *Nucl. Phys.* **B** **61**, 381 (1973).
- [49] LHCb collaboration R. Aaij et al. *Phys. Rev. Lett.* **115**, 072001 (2015).
- [50] Q. Wang, X.-H. Liu, and Q. Zhao. *Phys. Rev. D* **92**, 034022 (2015).
- [51] V. Kubarovsky and M.B. Voloshin. Formation of hidden-charm pentaquark in photon-nucleon collisions. *Phys. Rev. D* **92**, 031502 (2015).
- [52] Marek Karliner and Jonathan L. Rosner. Photoproduction of Exotic Baryon Resonances. *arXiv:1508.01496*.
- [53] S. Agostinelli et al. GEANT4: A simulation toolkit. *Nucl. Instrum. Meth.*, A506:250–303, 2003.
- [54] M. Ungaro. <https://gemc.jlab.org/gemc/html/index.html>.
- [55] R. Niyazov and S. Stepanyan. *CLAS-NOTE 2005-021* (2005).
- [56] HPS Proposal for 2014-2015 Run <https://confluence.slac.stanford.edu/display/hpsg/HPS+Proposals>.

- [57] A. Celentano et al. *EPJ Web of Conferences* **73**, 08004 (2014).
- [58] H. Fenker et al. BoNuS: Development and Use of a Radial TPC Using Cylindrical GEMs. *Nucl. Inst. and Meth. A* **592**, 273 (2008).
- [59] S. Stepanyan et al. <https://www.jlab.org/conferences/ehs-tsf/Stepanyan.pdf>.
- [60] K. Gnanvo et al. https://wiki.jlab.org/pcrewki/images/f/ff/KG_pRadReadinessReview_20160325.pdf.
- [61] K. Gnanvo et al. *Nucl. Inst. and Meth.* **A782**, 77 (2015).
- [62] SoLid collaboration. http://hallaweb.jlab.org/12GeV/SoLID/files/solid_precdr.pdf.
- [63] N. Liyanage. http://hallaweb.jlab.org/12GeV/SoLID/meeting_coll/2012_06_dryrun/SoLID_GEM_review_06_2012.pdf.
- [64] J.P. Wellisch. *arXiv:nucl-th/0306012* (2003).
- [65] Tetsuo Abe. GRAPE-Dilepton (version1.1), A Generator for Dilepton Production in ep Collisions. *arXiv:hep-ph/0012029*.
- [66] M. Sargsyan. *CLAS-NOTE 90-007* (1990).
- [67] M. Boer. Generator for DDVCS and TCS reactions.
https://hallaweb.jlab.org/wiki/index.php/DDVCS_and_TCS_event_generator.
- [68] J. Sakurai. *Phys. Rev. Lett.* **22**, p981 (1966).
- [69] S. Stepanyan. *Phase space event generator (Private communications)*.
- [70] CERN library program. *Lepto651 and Jetset74* (2005).
- [71] M. Holtrtop, J. Jaros, and S. Stepanyan. *Heavy Photon Experiment in Hall-B at Jefferson lab, E12-11-006* (2011).